Lasers in Manufacturing and Materials Processing
https://doi.org/10.1007/s40516-025-00313-9

RESEARCH

Surface Roughness Formation in Powder Bed Fusion of Copper Using Gaussian and Ring-Shaped Laser Beam Profiles

Alexander Bauch[1] · **Philipp Kohlwes**[1] · **Ingomar Kelbassa**[1,2]

Received: 13 June 2025 / Revised: 24 August 2025 / Accepted: 4 September 2025

Abstract

Both Gaussian laser beam profiles and ring-shaped laser beam profiles demonstrate the capability to produce specimens with a part density of more than 99.5% and an electrical conductivity above 99% compared to the International Annealed Copper Standard (IACS) in powder bed fusion of copper using a laser beam (PBF-LB/M/Cu). However, the influence of the beam profile on the surface roughness and surface characteristic has not yet been investigated in detail. In order to close this gap, inclined cube geometries are manufactured with varying laser power and scan speed using a Gaussian and ring-shaped beam profiles. The results reveal that the beam profile achieving the lowest surface roughness *Sa* in the investigated parameter range depends on the surface orientation. For the down-skin surfaces, the use of ring-shaped beam profiles reduces the surface roughness *Sa* by up to 29.9% compared to the Gaussian beam profile, whereas the surface roughness *Sa* for the up-skin and side surface is more than doubled. This is related to differences in surface roughness formation of the Gaussian and ring-shaped beam profiles, which are discussed in detail. For all investigated beam profiles, changes in the height of the peaks, depth of the valleys and the number of attached particles on the surface are observed with varying laser power and scan speed. Furthermore, a trend between the surface roughness *Sa* of the inclined cube geometry and the aspect ratio *R* of the weld geometry is found, indicating that the welding regime influences the surface roughness.

Keywords Additive manufacturing · Pure copper · Powder bed fusion using a laser beam · Beam shaping · Surface roughness

Extended author information available on the last page of the article

Published online: 12 September 2025

Introduction

Additive manufacturing (AM) technologies overcome existing conventional design restrictions and enable the production of application-specific designs. In powder bed fusion of metals using a laser beam (PBF-LB/M according to DIN EN ISO 52900), a component is produced by selectively melting a metal powder layer-wise using a laser beam based on a sliced Computer-Aided Design (CAD) model. In addition to the geometric accuracy and mechanical properties of the material, the surface quality is crucial for the use of these components. Investigations on the titanium alloy Ti6Al4V reveal that the fatigue strength at $3 \cdot 10^7$ cycles increases from 300 to 775 MPa by reducing the surface roughness *Ra* from 17.6 to 0.3 µm by milling [1]. However, tool accessibility is challenging for complex components like the ones manufactured via PBF-LB/M, especially in the case of inner channels. Utilizing an electropolishing process, the surface roughness *Ra* of cylindrical tubes of Hastelloy X with a 3 mm inner channel is reduced by more than 85% [2] Differences in the quality of the surface finishing between external and internal surfaces are reported for a stainless steel AISI 316 L component due to the accessibility of the counter electrode during electropolishing, while chemical polishing achieves a similar surface quality [3].

Post processing of inner channels is particularly relevant for copper applications, as it is widely used for heat sinks and heat exchangers consisting of complex channels. For example, the hydraulic pressure drop in a complex cooling channel made of CuCr1Zr increases from around 450 to 1350 mbar for a turbulent flow at a Reynolds number above 40,000 by changing the build orientation from 45° to 0° (horizontal) in relation to the substrate plate due to a decrease in surface quality and anisotropy [4]. Furthermore, pure copper is widely used for radio frequency (RF) cavities [5]. An improvement of the quality factor of a side-coupled cavity linac structure made of pure copper from 20 to 75% comared to the simulated quality factor is measured after post processing, which reduces the surface roughness Sq ranging from 22 to 30 to around 1 µm [5]. Overall, it can be stated that a uniform, smooth surface is preferable from an application perspective [1–5]. For this reason, the influence of the PBF-LB/M process on surface quality is subject of several publications.

Influence of the Part Orientation and Position on the Surface Roughness

Complex components consist of a variety of different oriented surfaces, which can be classified based on the component in the direction of the build direction (BD) $\overrightarrow{n_{BD}}$ of the normal vector $\overrightarrow{n}$ given by the inclination angle α between the horizontal plane and the surface plane, as shown in Fig. 1. An up-skin surface possesses a positive BD-component $\overrightarrow{n_{BD}}$ of the normal vector, while a down-skin surface possesses a negative BD-component $\overrightarrow{n_{BD}}$.

The down-skin surface roughness *Sa* increases from around 12 to 68 µm with a decreasing inclination angle from 75 to 30° for thin wall samples of AlSi10Mg [6]. Comparing the surface roughness of the up-skin surface and down-skin surface of Hastelloy X specimens at an inclination angle of 40°, with a measured surface roughness *Ra* of 28 µm for the up-skin surface and 45 µm for the down-skin surface, a higher surface roughness is evident for the down-skin surface compared to the up-

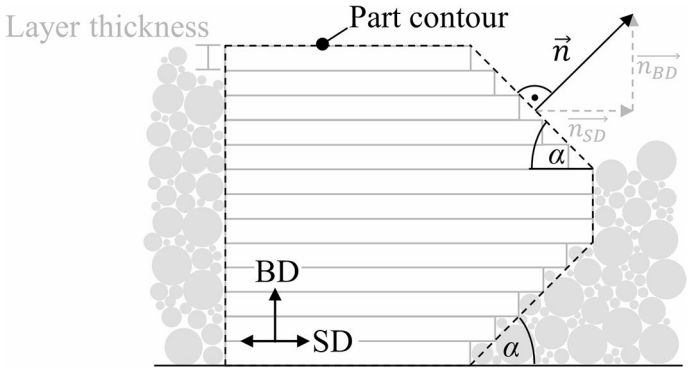

Fig. 1 Sketch of a component with the surface normal vector $\vec{n}$ given by the inclination angle α with a component along the build direction (BD) and scan direction (SD)

skin surface [7, 8]. In comparison, at an inclination angle of 80°, the surface roughness *Ra* is around 17 µm for both orientations, indicating a different sensitivity of the surface roughness to a decreasing inclination angle [7, 8].

3D surface images of inclined cubes of Hastelloy X reveal that the up-skin surface at an inclination angle of 45° does not only follows the sliced stair-case, but also comprises of peaks and valleys determined by the melt pool shape with attached particles mainly located between scan tracks, while the down-skin surface exhibit a strong adhesion of partially molten particles [2, 7]. The reason is the different heat conduction on these surfaces. While the heat for the up-skin surface is mainly conducted through the previously solidified layer, the down-skin surface is mainly surrounded by the powder bed, as shown in Fig. 1, and therefore the melt pool penetrates into the powder bed, resulting in heat conduction across loose powder particles [2, 7, 8]. For example for pure copper, the heat conductivity λ decreases by one order of magnitude from around 412 to 0.4 $\mathrm{W/(mK)}$ for loose powder with a particle size of 40 µm compared to pure copper samples produced via PBF-LB/M [9, 10]. The resulting heat accumulation leads to the sintering or partially melting of particles. Samples made from Hastelloy X at an inclination angle of 45°, confirm an increase in particle count on the down-skin surface with increasing volume energy density, for example for a particle size of 5 µm from about 480 to 800, with an increase in laser power from 200 to 370 W and an decrease in scan speed from 3000 to 2000 mm/s [7].

Considering the part orientation, a higher surface roughness *Ra* in the range of 19–41 µm compared to a surface roughness *Ra* in the range of 15–21 µm is found for the side surface towards the initial position of the recoater for cubes made of AlSi10Mg [11]. An increase in side surface roughness *Ra* from 19 to 29 µm along the recoating direction is also evident for cubes made of Amdry 1718 [12]. In-situ laser profilometry indicates a statistically significant correlation of the top surface roughness with the recoating speed in the range of 50–400 mm/s and the median particle size D50 in the range of around 14–42 µm, so that an increase in recoating speed and median particle size tends to increase the top surface roughness [13, 14]. Furthermore, the side surface roughness *Ra* rises from around 9 to 39 µm in the direction of the gas flow, which can be attributed to process related spatters [11]. This is consis-

tent with a study on process spatter of Hastelloy X, in which parts printed in spatter rich regions reveal a higher surface roughness *Sa* on the top surface in the range of 14.4–28 µm compared to parts printed in a low-spatter area with a surface roughness *Sa* of the top surface in the range of around 13–17 µm [15].

Overall, it can be concluded that the surface quality depends on the orientation of the surface, the recoating process, the gas flow as well as the process parameters, such as the laser power and scan speed [4–8, 11–13, 15–20].

Influence of the Process Parameters on the Surface Roughness of Pure Copper Samples

Pure copper samples with a density of larger than 99.7% and electrical conductivity of more than 99% compared to the International Annealed Copper Standard (IACS) can be produced either by using laser radiation with a wavelength of around 515 nm (green spectrum) and a laser power of up to 500 W or with a wavelength of around 1064 nm (near-infrared spectrum) and a laser power of up to 1 kW [9, 21]. The required increase in laser power with increasing wavelength of the laser radiation from 515 to 1064 nm is related to the drop in absorptivity of oxygen-free pure copper powder from 72 to 27% [22]. To compensate for the lower absorptivity, a keyhole welding process is used [23].

Using laser radiation of 515 nm wavelength, a side surface roughness *Ra* of 15.9 µm is achieved with two contour exposures for a 30 µm layer thickness, a laser power of 200 W and a scan speed of 600 mm/s [24]. Increasing the layer thickness to 40–60 µm raises the side surface roughness *Ra* to around 18–22 µm respectively [24]. Furthermore, the side surface roughness *Ra* increases from 15.9 to around 29 µm with an increase in laser power from 200 to 500 W at a layer thickness of 30 µm [24]. This is consistent with an observed increase in side surface roughness from around 14 to 22 µm with increasing volume energy density from around 200 to 500 J/mm³ [25].

Using laser radiation of 1064 nm wavelength, a top surface roughness *Ra* of around 18 µm at a laser power of 400 W, a scan speed below 500 mm/s and a hatch distance below 120 µm is reported [26]. However, increasing the scan speed to 600 mm/s increases the surface roughness of the top surface to more than 30 µm [26]. Another study found a surface roughness *Ra* of the top surface of around 13 µm at a line energy, given by the ratio of laser power and scan speed, of 0.5 J/mm for a hatch distance of 80 µm and a layer thickness of 30 µm [27]. In addition, an increase in surface roughness *Ra* of the top surface to 31.42 µm is observed for a decrease in line energy to 0.15 J/mm or to about 20 µm with increasing line energy to 1 J/mm [27]. For samples produced at a volume energy density (VED) of 583 J/mm³, in addition to the surface roughness *Ra* of the top surface of about 12 µm and the side surface of about 15 µm, a higher surface roughness *Ra* of about 15 µm is reported for the up-skin surface compared to the down-skin surface with a surface roughness *Ra* of 19 µm at an inclination angle of 45° [14, 28]. Considering the down-skin surface of RF cavities, an increase in surface roughness *Ra* from 27.6 to 33.8 and 34.8 µm is observed with decreasing inclination angle from 28 to 23 and 18° respectively [29].

Overall, the influence of the process parameters on the surface roughness of the top and side surface of pure copper samples using laser radiation with a wavelength

of around 515 and 1064 nm is subject of several studies [5, 9, 24–27]. However, there are no detailed investigations in the literature on the influence of the process parameters of the PBF-LB/M process on the surface characteristics of pure copper for the up-skin and down-skin surfaces.

Laser Beam Shaping for Pure Copper

A recent investigation demonstrates that pure copper specimens with a relative density of around 99.7% and an electrical conductivity of around 101.5%IACS can be produced by using near-infrared laser radiation with a ring-shaped beam profile at a laser power of 1300 W, a scan speed of 400 mm/s and a hatch distance of 140 µm [30]. Ring-shaped beam profiles consist of a Gaussian core and a surrounding ring and are characterized by their power ratio (core/ring). Changing the power ratio from 35/65 to 10/90, increases the number of lack-of-fusion pores and thus decreases the relative density from around 99.7 to 98.8% [30].Comparing the weld width and weld depth of single-tracks welded with a Gaussian beam profile and a ring-shaped beam profile with a power ratio of 35/65 at an identical laser power of 1000 W and a scan speed of 500 mm/s, a decrease of the weld width from around 210 to 190 µm and weld depth from around 460 to 60 µm is evident [30, 31]. Consequently, the aspect ratio R, given by the ratio of weld depth to weld width, decreases from more than 2 to less than 0.5, indicating a change in welding behavior from keyhole welding ($R > 0.8$) to heat conduction welding ($R < 0.5$) [31, 32].

For a Gaussian beam profile, the intensity peak in the center causes a outwards temperature gradient in the melt pool and thus an flow due to the Marangoni effect, pulling the melt outwards and a depression is formed in the center [33, 34]. In addition, vaporization and the inherent recoil pressure induces shear stresses on the melt pool surface, which contribute to the depression formation in the center [34, 35]. In contrast, the numeric simulation of single-tracks of Ti6Al4V using a ring-shaped beam profile with a power ratio of 0/100 reveals an annular depression zone at the intensity peak of the surrounding ring [36]. This cause a temperature gradient in the melt pool towards the center and thus an inward flow due to the Marangoni effect, forming a bulge in the center, which is confirmed by in-situ high-speed x-ray imaging [36]. At intermediate power ratios, the recoil pressure caused by the Gaussian core of the intensity distribution forms a further depression in the center, which counteracts the bulge formation [36].

The numerical simulation of single-tracks of different materials, including AlSi10Mg [35], Ti6Al4V [36] and AISI 316 L [37], reveal a lower maximum temperature and temperature gradient in the melt pool for ring-shaped beam profiles compared to a Gaussian beam profile. This finding is experimentally validated for AISI 316 L using multispectral imaging [38]. An altered microstructure, from close to polycrystalline to a high texture index, is found in Inconel 718 when ring-shaped beam profiles are employed due to the modified temperature gradient and melt pool geometry [39]. In addition, a decrease in vaporization by 40% is found for AlSi0Mg using a ring-shaped beam profile with a power ratio of 0/100 compared to a Gaussian beam profile [35]. In-situ high-speed x-ray imaging reveal that the metal vapor jet in the center drives process spatter in PBF-LB/M both directly and indirectly due to

an induced argon gas flow [40, 41]. High-speed imaging confirms an increase in the number of spatters per fused area for a Gaussian beam profile compared to a ring-shaped beam profile for Ti6Al4V at a laser power of 300 W by a factor in the range of 1.6–6.7, depending on the scan speed [42]. Overall, the change in the melt pool dynamics and the reduction of vaporization for ring-shaped beam profiles tends to enlarge the process window towards higher scan speeds and laser powers for AISI 316 L [43]. Furthermore, a wider but shallower melt pool geometry is reported for various materials using a ring-shaped beam profile in comparison to a Gaussian beam profile at similar laser power and scan speed [35–37, 39, 42].

Weld tracks of the aluminum alloy EN AW-5083 produced with ring-shaped laser beam profile reveal a higher roughness of the primary profile Pa for a Gaussian beam profile compared to a power ratio of 20/80 for all investigated laser powers in the range of 150–600 W and scan speeds in the range of 400–1000 mm/s [44]. For single-layer multi-track segments of AISI 316 L, a higher surface roughness *Ra* for a Gaussian beam profile compared to the investigated ring-shaped beam profiles is reported [43]. In contrast, cubic samples made of Inconel 718 show that the average of the side surface roughness *Sa* increases from around 11.3 to 11.6 µm when using a ring-shaped beam profile with an energy distribution of 10/90 instead of a Gaussian beam profile with the same volume energy density [45]. It should be noted that both the laser power and the hatch distance are increased for the ring-shaped beam profile, which may influence the surface roughness.

Although the application of ring-shaped beam profiles reveal a tendency towards a more stable welding process, the influence of ring-shaped laser beam profiles on the surface characteristics and the surface roughness formation of samples produced by PBF-LB/M has not yet been investigated in detail [30, 35–39, 42–45]. For the down-skin surface, the surface roughness is formed by the penetration of the melt pool into the powder bed [7, 8]. The authors hypothesize that the surface roughness reduces because the shallower melt pool of the ring-shaped beam profile compared to a Gaussian beam profile results in a lower penetration depth. In contrast, the surface roughness of an up-skin surface is formed by the stair-case effect and the shape of the weld face, which under ideal conditions becomes semicircular due to the surface tension [7, 8]. During cooling, the curvature of the weld face is influenced by a variety of forces, including buoyancy, gravity, capillary, Marangoni, and wetting forces [34, 46, 47]. As ring-shaped beam profiles tend to generate less vaporization, inherent recoil pressure and melt pool velocity compared to a Gaussian beam profile, the authors hypothesize a reduction of the surface roughness due to fewer shape deviations [35–38]. For the side surface, the weld seams are regularly stacked on top of each other [48]. For tubes made of AlSi10Mg and Inconel 718, the side surface roughness tends to decrease with increasing weld width, whereas a unstable contour melting tends to increase the surface roughness [48]. As ring-shaped beam profiles tend to produce a broader and more stable weld seam in comparison to Gaussian beam profile, the authors hypothesize that the surface roughness decrease.

Overall, the authors assume that the surface roughness is reduced by using ring-shaped beam profiles.

Objectives of the Study

Considering the previous literature review, four research gaps regarding the surface quality at different surface orientations of pure copper samples produced by the PBF-LB/M process can be identified, which will be addressed in this study:

1. The influence of the process parameters on the surface roughness and surface characteristics using a Gaussian beam profile.
2. The influence of the power ratio and process parameters on the surface roughness and surface characteristics using ring-shaped beam profiles.
3. The lowest achievable surface roughness of the Gaussian and ring-shaped beam profiles with regard to the surface orientation.
4. The surface roughness formation of the Gaussian and ring-shaped beam profiles with regard to the surface orientation.

In order to close this gaps, inclined cube geometries are manufactured with varying laser power and scan speed using a Gaussian beam profile and various ring-shaped beam profiles with different power ratios. Two contour exposures are used. The surface roughness of four different surface orientations is measured optically using confocal microscopy. The influence of the process parameters on the surface roughness are discussed separately for the Gaussian and ring-shaped beam profiles. The lowest achievable surface roughness and respective surface characteristics of the Gaussian and ring-shaped beam profiles are compared and discussed. The surface roughness formation of the Gaussian and a ring-shaped beam profile is examined with respect to the surface orientation using etched cross-sectional images.

Materials and Methods

Figure 2 shows the support-free, inclined cube geometry used in this study with top and side surface as well as up-skin and down-skin surface, covering typical surface orientations of complex components. For down-skin surfaces at an inclination angle below 40°, support structures are recommended for manufacturability [49]. For this reason, an inclination angle of 45° is selected for this study, which does not require any supports, alongside an inclination angle of 35°, which challenges the capability

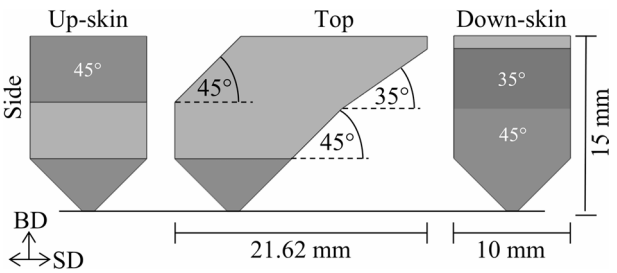

Fig. 2 Schematic representation of the sample geometry

of the PBF-LB/M process. Conversely, the inclination angle of the up-skin surface is non-critical for manufacturability. Therefore, only an inclination angle of 45° is selected for the comparison of the up-skin and down-skin surface. The side surface is chosen as it is typically investigated [11, 12, 14, 24, 25, 28]. The top surface is not examined in this study, as investigations indicate that a decrease in density tends to increase the surface roughness of the top surface and a density larger than 99.5% is not achievable for all ring-shaped beam profiles [6, 30].

The total height of the geometry is 15 mm, whereby the first 4 mm is designed as a truncated pyramid to achieve a steady state of the PBF-LB/M process and enable tool-free manual removal.

Specimens are manufactured using a commercial PBF-LB/M machine DMP Flex 350 (3D Systems Inc., USA) and spherical pure copper powder Cu OFHC (ECKART TLS GmbH, Germany). The copper powder has a purity larger than 99.95% and a particle size distribution in the range of around 15–45 µm (D10 - D90), measured by dynamic image analysis using a Camsizer X2 (Microtrac Retsch GmbH, Germany). The oxygen content of the virgin powder and after completion of all investigations (25 build jobs, 11 sieving cycles under argon atmosphere and a total of one year of storage) is 104 ± 2 and 257 ± 5 ppm respectively, measured by inert gas fusion using an Elementrac ONH-p 2 (Eltra GmbH, Germany). An oxygen content below 400 ppm complies with the standard for CU-ETP. Deoxidized, oxygen-free copper Cu-HCP is used as substrate material.

A meander hatching exposure strategy with two contour exposures is chosen, as outlined in Fig. 3. The cube samples are rotated by -15° relative to the build direction (z-axis) to avoid a parallel alignment of them to the recoater. A rotation angle of the scan direction between consecutive layers of 67° and a scan order from inside to outside (Hatch - C2 - C1) is defined. Two contour exposures are selected as previous studies for pure copper show that this achieves a minimum surface roughness *Ra* of 15.9 µm for the side surface [24].

The process parameter combination for the hatch is based on previous results for each beam profile. The beam profile is changed from experiment to experiment, resulting in a total of four build jobs without repetition. The process parameter combinations for the contour exposures are randomly assigned to the samples, which are arranged on the half of the building area facing the blower across the entire width of the building area.

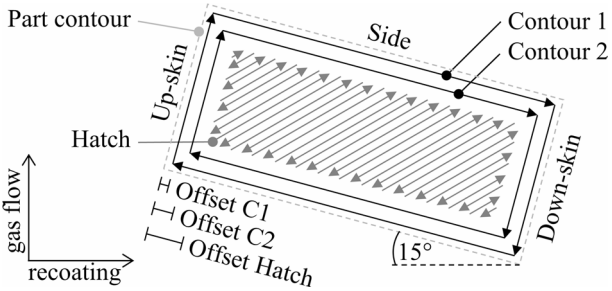

Fig. 3 Sketch of the exposure strategy consisting of the contour 1 (C1), contour 2 (C2) and the hatch

Table 1 Overview of the full-factorial experimental plan for the contour exposure using a Gaussian beam profile

Parameter		Limit		Step size
		Lower	Upper	
Laser power P	in W	500	1000	100
Scan speed v	in mm/s	400	800	100

Table 2 Overview of the full-factorial experimental plan for the contour exposure using ring-shaped beam profiles

Parameter		Limit		Step size
		Lower	Upper	
Laser power P	in W	1000	1300	100
Scan speed v	in mm/s	400	900	100

For all experiments, a layer thickness of 45 µm is defined and no preheating is used. The recoating speed is 115 mm/s and the blower speed (gas flow) is 2.6 m/s. The oxygen content of the inert argon atmosphere within the build chamber ranges between 3.5 and 20.3 ppm.

Gaussian Beam Profile

Initially, the laser system installed as standard, a 1 kW fiber laser (IPG Laser GmbH, Germany) emitting laser radiation of 1070 nm wavelength is used. The limits and step sizes of the full factorial experimental plan for the contour exposure, given in Table 1, are selected based on previous investigations. The offset C1, C2 and Hatch is set to 0, 140 and 280 µm respectively.

Ring-Shaped Beam Profile

In order to investigate the influence of process parameters and ring-shaped beam profiles on the surface roughness, the PBF-LB/M machine is equipped with a programmable fiber laser AFX-1500 (nLIGHT Inc., USA) emitting laser radiation of 1070 nm wavelength. The laser system provides seven switchable ring-shaped beam profiles with defined power ratios (core/ring) with a maximum laser power inside the build chamber of around 1350 W, measured with a calorimetric EC-PowerMonitor (Primes GmbH, Germany). The limits and step sizes of the full factorial experimental plan, given in Table 2, are selected based on process maps of single-tracks [30]. Three different ring-shaped beam profiles with power ratios of 35/65, 20/80 and 10/90 are selected for the investigations and the experimental plan is run for each ring-shaped beam profile. The offset C1, C2 and Hatch is set to 0, 180 and 360 µm respectively.

Intensity Distributions

Laser beam profile measurements are carried out with a laser power of up to 200 W using a CCD camera SP928 (Ophir Spiricon Europe GmbH, Germany). A beam splitter LBS-300 ensures that only 0.01% of the input laser radiation is directed onto the CCD-chip and is further attenuated by two neutral density filters with a total of ND4 (Ophir Spiricon Europe GmbH, Germany). The laser beam intensity distributions along the major axis of the investigated beam profiles scaled to a laser power of

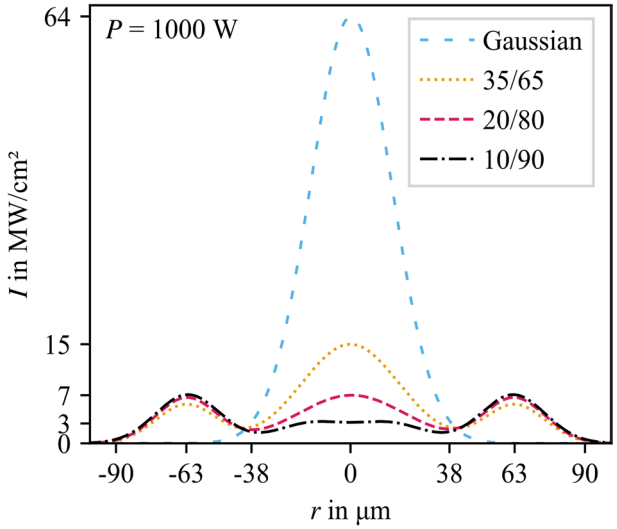

Fig. 4 Fitted laser beam intensity I as a function of the radius r along the major axis for the investigated beam profiles scaled to a laser power P of 1000 W

Table 3 Overview of the calculated beam diameters based on the measured intensity distributions for all investigated beam profiles

Parameter			Power ratio			
			Gaussian	35/65	20/80	10/90
Image			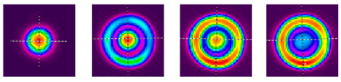			
Beam diameter	$D_{4\sigma}$	in µm	62.60	159.45	171.18	178.12
	$D_{1.5}$	in µm	85.77	164.33	165.93	167.54

1000 W are shown in Fig. 4. For the Gaussian beam profile, a Gaussian distribution is fitted to the measurement data. For the ring-shaped beam profiles an axisymmetric beam profile consisting of a Gaussian core and two radially shifted Gaussian distributions are used [30, 50]. A decrease in peak intensity is evident as the beam profile changes from Gaussian to a ring-shaped beam profile.

Table 3 lists the respective beam diameters $D_{4\sigma}$, calculated by the second moment method according to DIN EN ISO 11,146, and $D_{1.5}$, which refers to an intensity threshold of 1.5 MW/cm², of all investigated beam profiles. The beam diameter $D_{4\sigma}$ of the ring-shaped beam profiles is around 2.5–2.8 times the beam diameter $D_{4\sigma}$ of the Gaussian beam profile. Furthermore, there is a difference of more than 10% between the beam diameters $D_{4\sigma}$ of the ring-shaped beam profiles due to the influence of the outwards intensity on the calculation. In contrast, considering a certain intensity of for example 1.5 MW/cm², there is a difference of less than 2% between the respective beam diameters $D_{1.5}$ of the ring-shaped beam profiles. For this reason, the authors assume a comparable interaction time for the ring-shaped beam profiles. However, the beam diameter $D_{1.5}$ of the Gaussian beam profile is approximately

half of the ring-shaped beam profiles. As comparable beam diameters are required to isolate the effect of the beam shape [47], the Gaussian and ring-shaped beam profiles are examined separately and subsequently compared.

Surface Roughness Measurement

The surface roughness is measured optically using a 3D laser scanning microscope VK-X3000 (Keyence Deutschland GmbH, Germany) utilizing a 20x objective. A stitched image composed of 2×3 images is used to obtain a representative evaluation area of 1×1 mm². Five measurements are performed on each surface and their numbering and positions are shown in Fig. 5. The orientation of the measured surface in relation to the gas flow and recoater is shown in Fig. 3. For the side surface, the downwind surface in the direction of the gas flow is selected, as a decrease in surface roughness is expected [11, 15].

The calculation of the area roughness is performed in accordance to DIN EN ISO 25178 using the VK-X3000 MultiFileAnalyzer software (Keyence Deutschland GmbH, Germany). Small-scale components are filtered by a S-filter of 2.5 µm and large-scale components by a L-filter of 1 mm. The S-filter is selected to be at least three times the measurement resolution in the x-y direction. The L-filter is adjusted to the size of the evaluation area, as this defines the long wavelength limit. A plane tilt correction is applied as F-operator.

In this study, the authors refer to the average value of the arithmetic mean height of the five measurements as the surface roughness *Sa* of the surface, whereas the mean value of the surface roughness $\overline{Sa}$ applies only to the main effect diagrams.

Cross-Sectional Images

In order to study the surface roughness formation of the different surface orientations, selected cube geometries are hot mounted, ground to the center using silicon carbide grinding paper, polished with diamond suspension (Struers GmbH, Germany) and etched in a hot ammonium persulfate solution (10%) to reveal the microstructure. Cross section images are taken using an inverted optical microscope GX-51 equipped with a UC30 camera (Olympus Europa SE & Co. KG, Germany). Differential interference contrast microscopy using a Nomarski differential interference contrast prism U-DICR sandwiched between two polarization filters GX-PO and GX-AN is

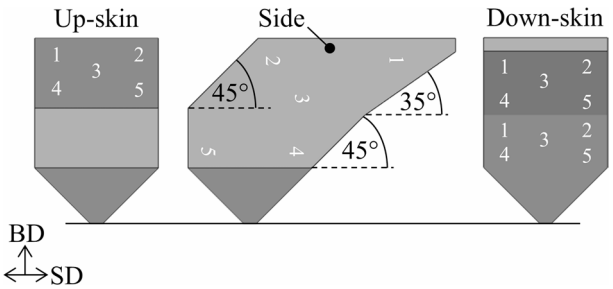

Fig. 5 Schematic representation of the sample geometry and the measuring points on the surfaces

employed to improve the visibility of the solidification lines (Olympus Europa SE & Co. KG, Germany).

Results

The experimental results of the surface roughness measurements for the Gaussian and ring-shaped beam profiles as a function of the process parameters are presented in the following. The arithmetic mean height *Sa* is selected for the analysis, as comparability with tactile measurements of the line roughness *Ra* is reported by Tan et al. [6], allowing comparability across literature. The maximum height *Sz* is not discussed in detail, as a linear relationship between the maximum height *Sz* and the arithmetic mean height *Sa* of all measurement points with a coefficient of determination of $R^2 = 0.93$ and a root mean square error of 17.16 µm is found, as shown in Fig. 6 in the appendix.

Gaussian Beam Profile

In Fig. 7, the mean value of the surface roughness $\overline{Sa}$ and its respective standard deviation is plotted as a function of the laser power *P* (Fig. 7a) the scan speed *v* (Fig. 7b) for the investigated surface orientations. In order to reveal the respective trend, a linear regression is used for the laser power, whereas a quadratic function is used for the scan speed, as an inflection point is recognizable. Furthermore, exemplary intensity images as well as three-dimensional representations of the different surface orientations are shown in Fig. 8 at a laser power of 500 and 1000 W as well as a scan speed of 400, 600 and 800 mm/s. The build direction (BD) and scan direction (SD), referring to the exposure plane of each layer, are indicated.

The highest total average of the surface roughness $\overline{Sa}$ of about 49 µm is observed for the down-skin at an inclination angle of 35°, followed by the down-skin at an inclination angle of 45° at around 42 µm. The up-skin and the side surface exhibit a lower total average of the surface roughness $\overline{Sa}$ of around 19 µm and 17 µm respectively.

Considering the linear trend lines in Fig. 7a, the following trends with increasing laser power from 500 to 1000 W are evident. For the down-skin surface at an inclina-

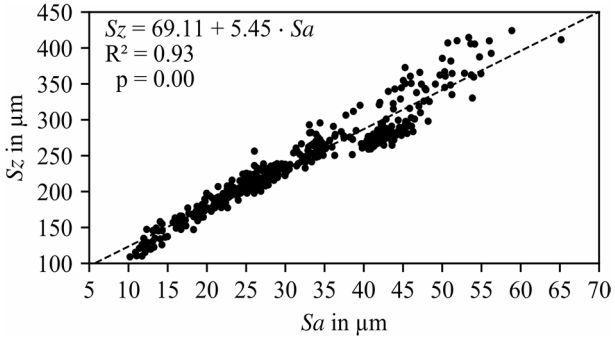

Fig. 6 Maximum height *Sz* as a function of the arithmetic mean height *Sa* of all specimens

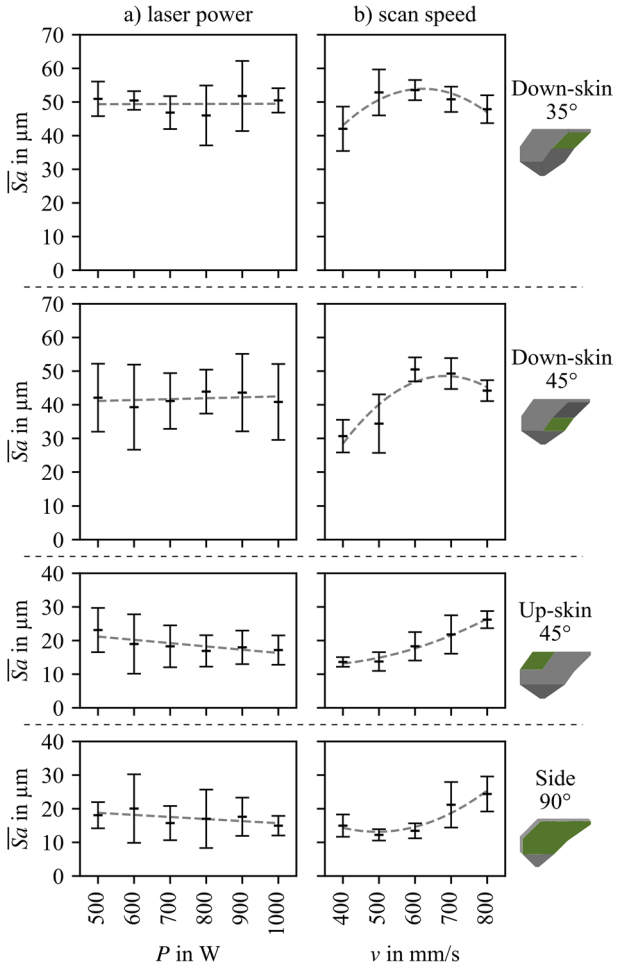

Fig. 7 Mean surface roughness $\overline{Sa}$ of all investigated surface orientations as a function of (a) laser power P and (b) scan speed v for the Gaussian beam profile

tion angle of 35°, there is no trend visible. However, a minimum surface roughness $\overline{Sa}$ of around 46 µm is found at a laser power of 800 W. For the down-skin surface at an inclination angle of 45°, a slight trend towards increasing surface roughness is noticeable, with a minimum surface roughness $\overline{Sa}$ of around 39 µm at a laser power of 600 W, whereas for the up-skin surface at an inclination angle of 45°, the surface roughness $\overline{Sa}$ decreases from around 23 to 17 µm. However, it must be noted that the surface roughness $\overline{Sa}$ for a laser power in the range of 600 to 1000 W varies closely in the range of 17–19 µm. For the side surface a tendency towards decreasing surface roughness $\overline{Sa}$ from 18 to 15 µm is evident with increasing laser power from 500 to 1000 W.

Figure 7b shows a maximum surface roughness $\overline{Sa}$ of around 54 and 50 µm for the down-skin surface at an inclination angle of 35° and 45° at a scan speed of 600 mm/s.

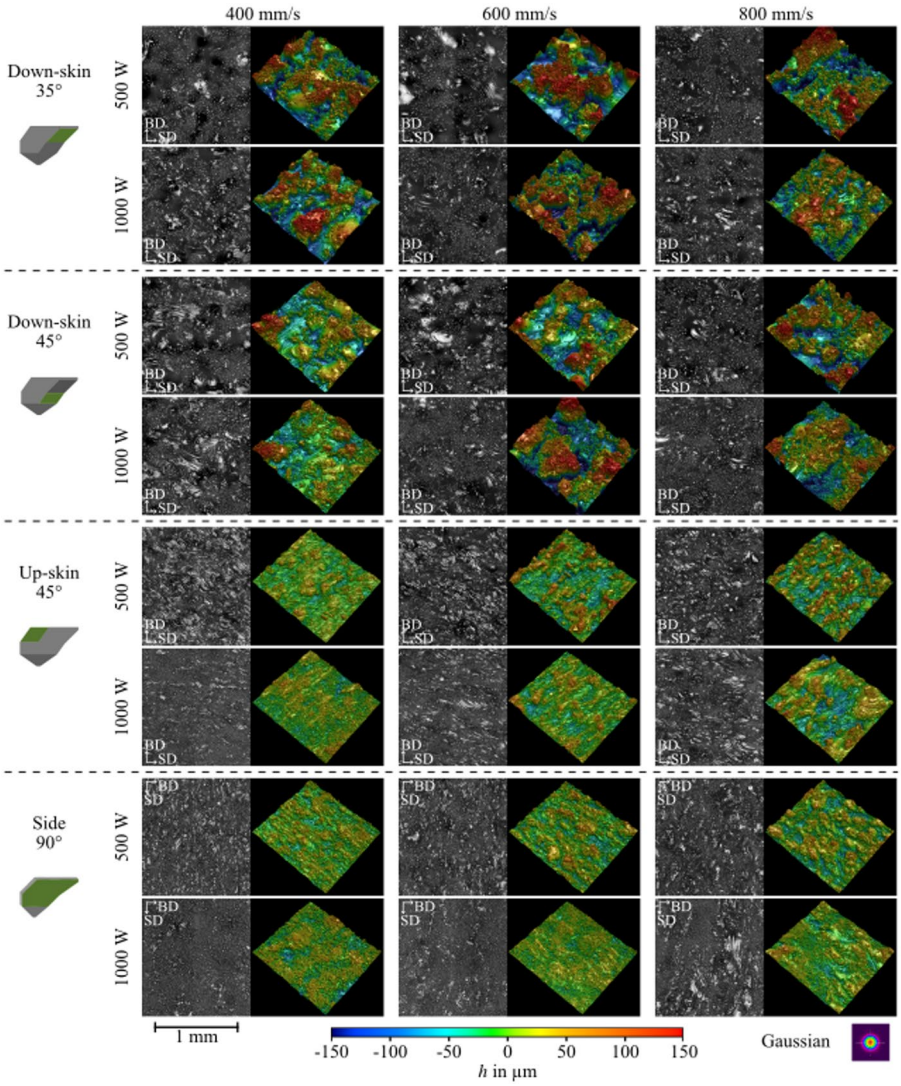

Fig. 8 Exemplary intensity images and three-dimensional representations at a laser power of 500 and 1000 W and a scan speed of 400, 600 and 800 mm/s for the Gaussian beam profile

A decrease in surface roughness $\overline{Sa}$ is evident both with decreasing scan speed to 400 mm/s and with increasing scan speed to 800 mm/s. At inclination angles of 35° and 45°, the lowest surface roughness $\overline{Sa}$ is around 42 and 31 µm respectively at a scan speed of 400 mm/s. For the up-skin surface an increase of the surface roughness $\overline{Sa}$ from 13 to 26 µm is found with increasing scan speed from 400 to 800 mm/s. However, only a minor increase of the surface roughness $\overline{Sa}$ of 0.12 µm is observed with increasing scan speed from 400 to 500 mm/s. The minimum surface roughness $\overline{Sa}$ for the side surface is approx. 12 µm at a scan speed of 500 mm/s. An increase in surface roughness $\overline{Sa}$ is evident both with decreasing scan speed to 400 mm/s as well

as increasing scan speed to 800 mm/s with a surface roughness $\overline{Sa}$ of around 14 and 26 µm respectively.

The intensity images as well as three-dimensional representations in Fig. 8 of the down-skin surface at an inclination angle of 35° exhibits peaks and valleys as well as attached particles, whereby the particles primarily adhere to the peaks. The intensity images show that the entire surface is covered with powder particles apart from the valleys where the bare surface and some solidification lines of the melt pool are visible. As the laser power increases from 500 to 1000 W, the height of the peaks remains constant, and thus no trend is evident in the main effect diagram in Fig. 7a. However, the valleys become narrower. In contrast, the height of the peaks and depth of the valleys increases with rising scan speed from 400 to 600 mm/s, which leads to an increase in surface roughness $\overline{Sa}$. A further increase in scan speed to 800 mm/s reduces the height and depth of the peaks and valleys respectively, decreasing the surface roughness $\overline{Sa}$.

Compared to the down-skin surface at an inclination angle of 35°, the spread between the peaks and valleys is reduced for the down-skin surface at an inclination angle of 45°, resulting in a lower surface roughness $\overline{Sa}$. Furthermore, slightly larger bare surface areas with more pronounced solidification lines are visible at scan speeds of 400 and 600 mm/s. However, the surface characteristics exhibit a change with increasing laser power from 500 W to 1000 W or scan speed from 400 to 800 mm/s similar to the down-skin surface at an angle of 35°. Consequently, the trend in the main effect diagram in Fig. 7 is the same.

For the up-skin surface at an inclination angle of 45°, a pronounced layer pattern is observed along the build direction for a laser power of 500 W and a scan speed of 400 mm/s. Furthermore, solidification lines are evident along the scan direction, as well as some peaks with attached particles. As the laser power increases from 500 to 1000 W, the height of the peaks decreases and the surface is more densely covered with particles, reducing the surface roughness $\overline{Sa}$. In contrast, rising the scan speed from 400 to 600 and 800 mm/s increases the quantity and height of the peaks as well as the depth of the valleys, raising the surface roughness $\overline{Sa}$.

Compared to the up-skin surface, considerably more attached particles are visible on the side surface, thus less solidification lines are recognizable along the scan direction. However, a layer wise pattern along the build direction remains observable. Similar to the up-skin surface, an increase in laser power from 500 to 1000 W results in an increase in the number of attached particles, while the height of the peaks declines. In addition, an increase in both the quantity and height of the peaks as well as the depth of the valleys is also evident with increasing scan speed from 400 to 800 mm/s. Consequently, the trend in the main effect diagram in Fig. 7 is similar.

Ring-Shaped Beam Profile

In Fig. 9a, the mean value of the surface roughness $\overline{Sa}$ and its respective standard deviation is plotted as a function of the power ratio of the ring-shaped beam profiles for the investigated surface orientations. Furthermore, exemplary intensity images as well as three-dimensional representations of the surfaces for a power ratio of 35/65 (Fig. 9b), 20/80 (Fig. 9c) and 10/90 (Fig. 9d) are shown at a laser power P of 1300 W

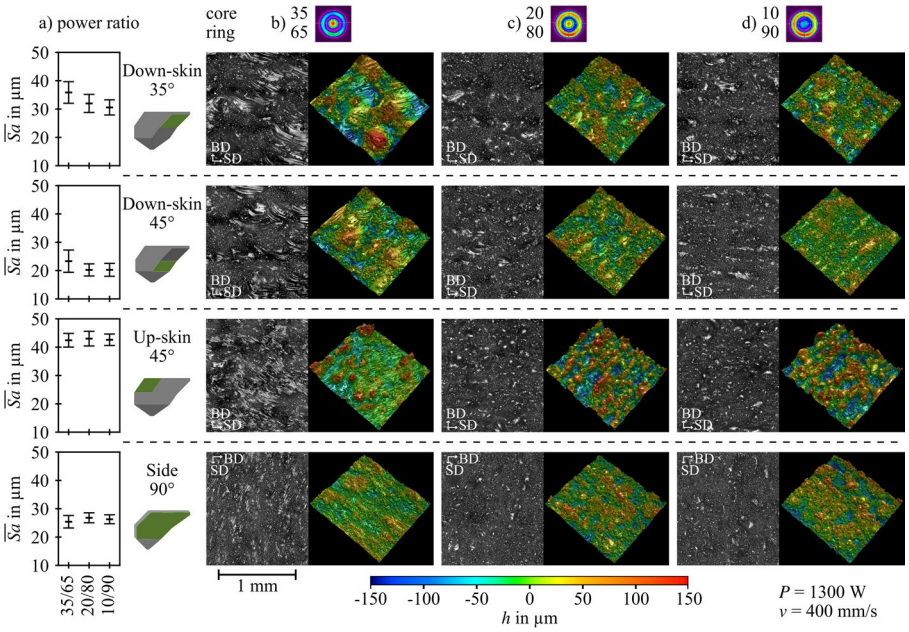

Fig. 9 **a**) Mean surface roughness $\overline{Sa}$ as a function of the power ratio for all investigated ring-shaped beam profiles and surface orientations. Exemplary intensity images and three-dimensional representations for a power ratio of **b**) 35/65, **c**) 20/80 and **d**) 10/90 at a laser power P of 1300 W and a scan speed v of 400 mm/s

and a scan speed v of 400 mm/s. This combination of process parameters is selected as it shows the most distinct differences in surface characteristics between the power ratio 35/65 to 20/80 and 10/90. The build direction (BD) and scan direction (SD), referring to the exposure plane of each layer, are indicated.

Considering the main effect diagram of the power ratio in Fig. 9a, a decrease in surface roughness $\overline{Sa}$ of the down-skin surface at an inclination angle of 35° from around 36 to 32 and 31 µm is evident by changing the power ratio from 35/65 to 20/80 and 10/90 respectively. A similar trend is observed for the down-skin surface at an inclination angle of 45°, for which the surface roughness $\overline{Sa}$ decreases from around 23 µm for a power ratio of 35/65 to around 20 µm for a power ratio of 20/80 and 10/90. For the up-skin surface at an inclination angle of 45°, there is only a small difference in the main effect diagram, as the surface roughness $\overline{Sa}$ is in the range of 42–43 µm for all power ratios. However, the power ratio of 20/80 exhibits the highest surface roughness $\overline{Sa}$ among these. For the side surface, the power ratio of 35/65 has the lowest surface roughness $\overline{Sa}$ of around 25 µm, whereas the power ratios of 20/80 and 10/90 have a surface roughness $\overline{Sa}$ of around 27 and 26 µm.

For the down-skin surface at an inclination angle of 35°, the intensity images as well as three-dimensional representations in Fig. 9b-d show a change in surface characteristic with altering power ratio. At the power ratio of 35/65, a layer wise pattern along the build direction and solidification lines of the melt pool are visible on the bare surface. Furthermore, a wavy surface structure is recognizable with particles

primarily attached to the peaks. However, some particles are also found all over the weld tracks. For the power ratios 20/80 and 10/90, no wavy surface structure is visible and the surface is largely covered with particles. In addition, a few peaks and narrow valleys without attached particles are visible.

Increasing the inclination angle of the down-skin to 45° reduces the height and depth of the peak and valleys and thus the surface roughness $\overline{Sa}$ for all power ratios in Fig. 9a. An increase in the number of attached particles is observed and in particular for the power ratio of 10/90 a uniform coverage of the surface with particles is evident. For the power ratio of 35/65 and 10/90, a layered pattern along the build direction is also noticeable.

A pronounced layer pattern along the build direction with clearly recognizable solidification lines is also evident for the up-skin surface at an inclination angle of 45° and a power ratio of 35/65. In addition, some narrow peaks with attached particles are visible. For a power ratio of 20/80 and 10/90, the quantity of these peaks increases noticeably, covering a large proportion of the surface. In addition to the rather spherical peaks, drop-shaped or cylindrical peaks are visible for a power ratio of 20/80 and 10/90. A major difference to the power ratio of 35/65 is that almost no particles adhere to these peaks, but rather adhere to the valleys between the peaks, leaving no solidification lines visible.

For the side surface, a rather wavy surface characteristic is visible for the power ratio of 35/65, whereas distinct valleys are evident for a power ratio of 20/80 and 10/90. Some solidification lines are visible along the scan direction at a power ratio of 35/65, while these are completely covered with particles for a power ratio of 20/80 and 10/90, with only a few peaks protruding without attached particles.

Overall, the surface characteristics of the ring-shaped beam profiles with a power ratio of 20/80 and 10/90 are similar at a laser power of 1300 W and a scan speed of 400 mm/s, whereas the power ratio of 35/65 show a distinct difference. In Fig. 10, intensity images and three-dimensional representations of the up-skin surface at an inclination angle of 45° are shown for a laser power P of 1200 and 1300 W and a scan speed v of 400 and 500 mm/s. A notable decrease in the number of peaks and attached particles is evident for a power ratio of 35/65, either with an increase in laser power from 1200 to 1300 W at a constant scan speed of 400 mm/s, or with a decrease in scan speed from 500 to 400 mm/s at a constant laser power of 1300 W. For a laser power below 1300 W or a scan speed above 400 mm/s, the surface characteristics, consisting of rather spherical peaks, drop-shaped or cylindrical peaks with attached particles in the valleys, are comparable across all investigated power ratios.

The same thresholds of laser power and scan speed apply also for the side surface. A decline in the number of peaks and attached particles is also found for the side surface, although almost half of the surface remains covered with particles in contrast to the up-skin surface in Figs. 9b and 10.

For the down-skin surface at an inclination angle of 35° and 45°, a change in surface characteristics occurs when the laser power increases from 1200 to 1300 W at a scan speed of 400 mm/s or when the scan speed decreases from 600 to 400 mm/s at a laser power of 1300 W. The most notable change in surface characteristics is the reduction in particle attachment compared to Fig. 9b, which improves visibility of broader peaks and valleys, while their height and depth remain almost unchanged.

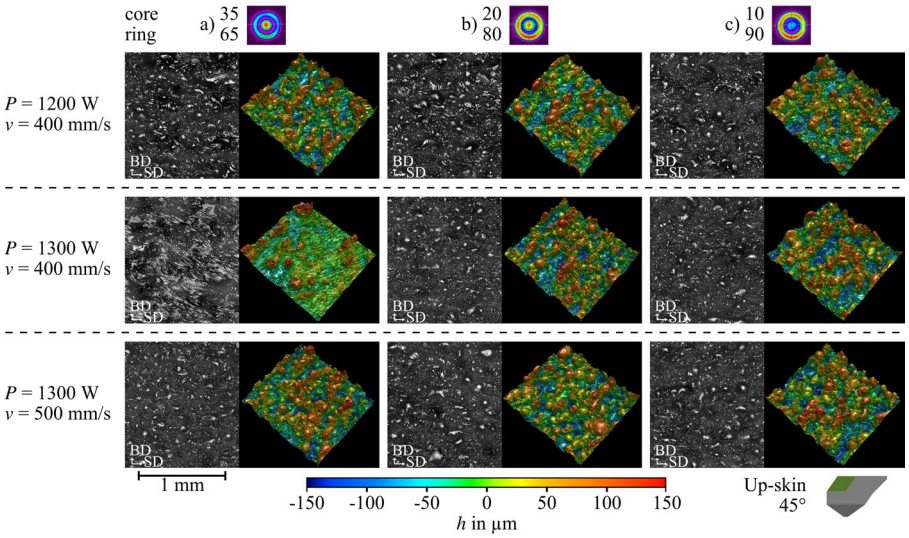

Fig. 10 Intensity images and three-dimensional representations of the up-skin surface at an inclination angle of 45° for the ring-shaped beam profiles with a power ratio of **a)** 35/65, **b)** 20/80 and **c)** 10/90 for different process parameter combinations

Overall, a transition of the surface characteristics only occurs for a power ratio of 35/65 at a laser power above 1200 W and a scan speed below 500 mm/s, so that all but one of the parameter combinations investigated using ring-shaped beam profiles have similar surface characteristics. Figure 11 presents the mean value of the surface roughness $\overline{Sa}$ and its respective standard deviation as a function of the laser power (Fig. 11a) and the scan speed (Fig. 11b) for the investigated surface orientations. In order to reveal the respective trend, a linear trend line is used.

For the down-skin surfaces at an inclination angle of 35° and 45°, a total average of the surface roughness $\overline{Sa}$ of around 33 and 21 µm is found. The up-skin and the side surface exhibit a total average of the surface roughness $\overline{Sa}$ of around 43 and 26 µm respectively.

Considering the linear trend lines in Fig. 11a, the following trends with increasing laser power from 1000 to 1300 W are evident. For the down-skin surface at an inclination angle of 35°, a decrease in surface roughness $\overline{Sa}$ from around 34 to 32 µm is visible, whereas at an inclination angle of 45° only a decrease of around 0.5 µm down to 21 µm is found. In contrast, the surface roughness $\overline{Sa}$ for the up-skin surface at an inclination angle of 45° increases from around 41 to 43 µm. A similar trend is apparent for the side surface. The lowest surface roughness $\overline{Sa}$ of around 25 µm is found at a laser power of 1000 W, increasing to 27 and 26 µm for a laser power of 1200 and 1300 W.

Figure 11b shows a maximum surface roughness $\overline{Sa}$ of around 35 µm for the down-skin surface at an inclination angle 35° and a scan speed of 700 mm/s. A decrease in surface roughness $\overline{Sa}$ to around 31 and 34 µm is evident with decreasing scan speed to 400 mm/s or with increasing scan speed to 800 mm/s respectively. The minimum surface roughness $\overline{Sa}$ of around 29 µm is found at a scan speed of 500 mm/s. A

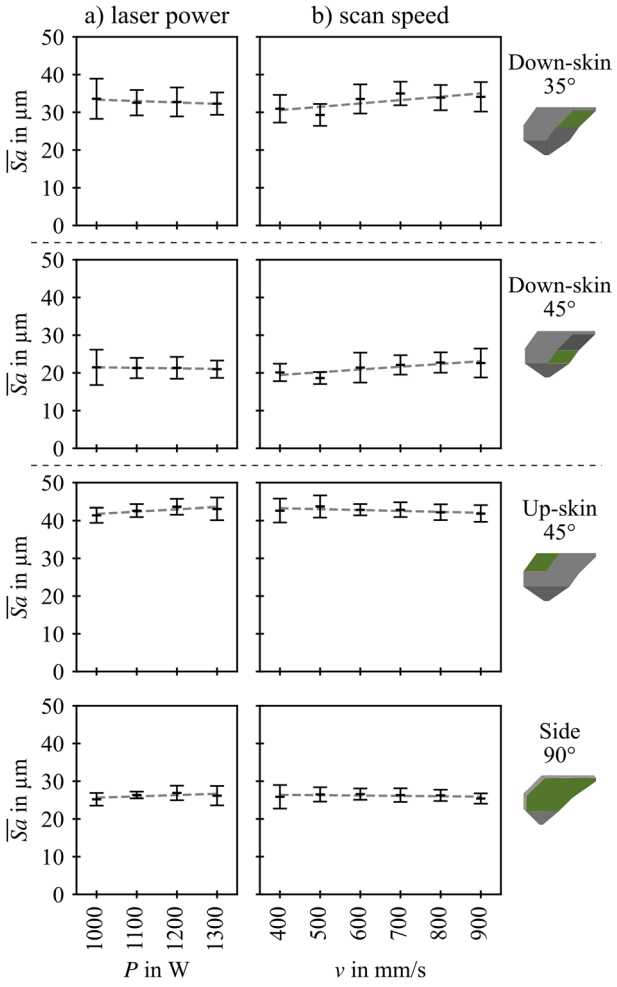

Fig. 11 Mean surface roughness $\overline{Sa}$ of all investigated surface orientations as a function of (a) laser power P and (b) scan speed v for all examined ring-shaped beam profiles

comparable trend with a maximum surface roughness $\overline{Sa}$ of around 23 µm and a minimum surface roughness $\overline{Sa}$ of approx. 19 µm is found for the down-skin surface at an inclination angle of 35°. In contrast, a decreasing trend is visible for the up-skin surface at an inclination angle of 45°. However, only minor changes are found with increasing scan speed from 400 to 900 mm/s and the surface roughness $\overline{Sa}$ is in the range of 42–44 µm. A comparable trend is visible for the side surface with a surface roughness $\overline{Sa}$ in the range of 25–27 µm.

Given that the majority of the parameter combinations examined using ring-shaped beam profiles exhibit comparable surface characteristics, the ring-shaped profile with a power ratio of 20/80 is selected to unveil the influence of the process parameter on the surface characteristics. Exemplary intensity images as well as three-dimensional

representations of the surfaces at a laser power of 1000 and 1300 W at a scan speed of 400 and 900 mm/s are shown in Fig. 12.

For the down-skin surface at an inclination angle of 35°, the height of the peaks and depth of the valleys does not change with increasing laser power from 1000 to 1300 W. However, a slight enlargement of the areas free of attached particles is noticeable, which may explain the slight decrease in surface roughness $\overline{Sa}$ with increasing laser power in the main effect diagram in Fig. 11a. In contrast, Fig. 12 revels an increase in the height of the peaks and depth of the valleys with rising scan speed from 400 to 900 mm/s, raising the surface roughness $\overline{Sa}$.

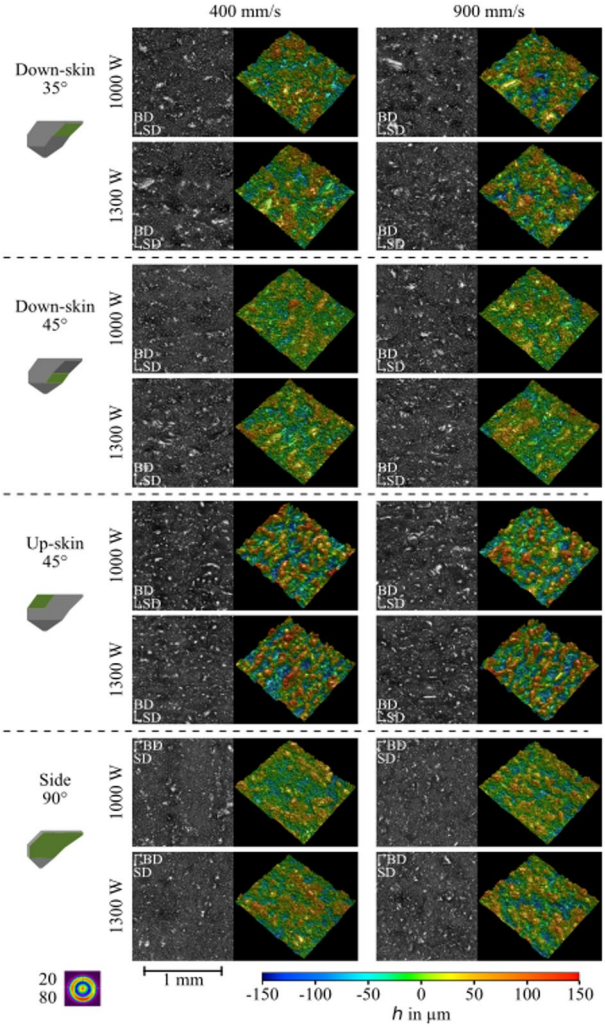

Fig. 12 Exemplary intensity images and three-dimensional representations of all surface orientations for the ring-shaped beam profile with a power ratio of 20/80 at a laser power of 1000 and 1300 W and a scan speed of 400 and 900 mm/s

Compared to the down-skin surface at an inclination angle of 35°, the down-skin surface an inclination angle of 45° exhibits shallower peaks, resulting in a lower surface roughness $\overline{Sa}$. The surface characteristics changes with increasing laser power from 1000 W to 1300 W or scan speed from 400 to 900 mm/s similar to the down-skin surface at an angle of 35°. Consequently, the trend in the main effect diagram in Fig. 11 is the same.

For the up-skin surface at an inclination angle of 45°, the number of peaks and particles attached to the valleys remains almost constant when the laser power is increased from 1000 to 1300 W. However, a minor increase in the height of the peaks is evident, which raises the surface roughness $\overline{Sa}$ slightly. This is also evident in Fig. 12 with increasing scan speed from 400 to 900 mm/s. However, the main effect diagram in Fig. 11b shows almost no influence of the scan speed on the surface roughness $\overline{Sa}$.

Compared to the up-skin surface, the side surface exhibits significantly shallower peaks and valleys. Furthermore, the number of peaks decreases, resulting in a lower surface roughness $\overline{Sa}$. The height of the peaks increases with increasing laser power from 1000 to 1300 W or scan speed from 400 to 900 mm/s, similar to the up-skin surface, resulting in a comparable trend in the main effect diagram in Fig. 11.

Comparison of Gaussian and Ring-Shaped Beam Profiles

In Fig. 13a, the lowest measured surface roughness *Sa* and its respective standard deviation is shown for each beam profile for all investigated surface orientations. Furthermore, intensity images as well as three-dimensional representations of the respective surfaces using the Gaussian beam profile (Fig. 13b) and the ring-shaped beam profile at a power ratio of 20/80 (Fig. 13c) are shown, as the most distinct difference in surface roughness is apparent between those beam profiles. In addition, the corresponding process parameters are specified.

For the down-skin surface at an inclination angle of 35°, the highest surface roughness *Sa* of around 33 µm is found in Fig. 13a for the Gaussian beam profile, whereases the lowest surface roughness *Sa* of around 25 µm is evident for the ring-shaped beam profile with a power ratio of 10/90. A similar trend is observed for the down-skin surface at an inclination angle of 45°, at which the Gaussian beam profile achieves a surface roughness *Sa* of around 23 µm, whereas the ring-shaped beam profiles with a power ratio for 20/80 and 10/90 result in a surface roughness *Sa* of around 16 µm. In contrast, the up-skin surface at an inclination angle of 45° shows a reverse trend. The Gaussian beam profile achieves the lowest surface roughness *Sa* of around 12 µm, while the highest surface roughness *Sa* of 39 µm is found for the ring-shaped beam profile with a power ratio of 10/90. This trend is also evident for the side surface. For the side surface, the Gaussian beam profile achieves the lowest surface roughness *Sa* of around 10 µm, whereas the highest surface roughness *Sa* of around 24 µm is achieved for the ring-shaped beam profile with a power ratio of 20/80.

Overall, the ring-shaped beam profiles with a power ratio of 20/80 and 10/90 result in a more or less comparable surface roughness $\overline{Sa}$, whereas a distinct difference is found compared to the Gaussian beam profile. The surface roughness *Sa* for a ring-shaped beam profile with a power ratio of 35/65 is in between the Gaussian beam

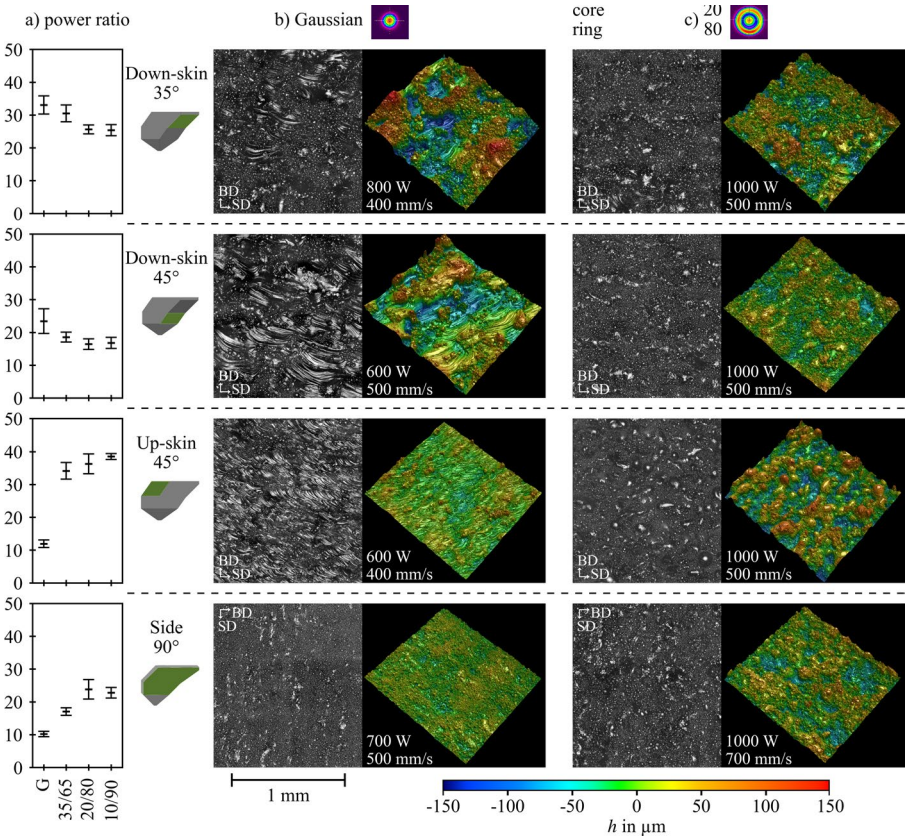

Fig. 13 **a**) Lowest measured surface roughness *Sa* for each surface orientation as a function of the beam profile. Exemplary intensity images and three-dimensional representations of **b**) the Gaussian beam profile and **c**) the ring-shaped beam profile with a power ratio of 20/80 of the respective surface

profile and the other two ring-shaped beam profiles. For the down-skin surfaces, ring-shaped beam profiles achieve a lower surface roughness *Sa* compared to the Gaussian beam profile, whereas the opposite applies for up-skin and side surfaces.

Comparing the intensity images and three-dimensional representations of the Gaussian beam profile and the ring-shaped beam profile at a power ratio of 20/80 in Fig. 13b and c, a distinct difference in the surface characteristics is also evident.

For the down-skin surface at an inclination angle of 35°, a wavy surface characteristic consisting of peaks with attached particles and bare valleys with visible solidification lines is evident for the Gaussian beam profile. In comparison, the surface of the ring-shaped beam profile with a power ratio of 20/80 is more densely covered with particles. In addition, a less wavy surface characteristic with shallower peaks and valleys is observed, reducing the surface roughness *Sa*.

As the inclination angle increases from 35° to 45°, a decrease in height of the peaks and depth of the valleys is observed for both the Gaussian and the ring-shaped beam profile with a power ratio of 20/80, resulting in a lower surface roughness *Sa*. In addition, a decrease in the number of attached particles is observed for the Gaussian

beam profile, while no distinct change is noticeable for the ring-shaped beam profile with a power ratio of 20/80.

For the up-skin surface at an inclination angle of 45°, the Gaussian beam profile produces a pronounced layer pattern along the build direction with only a few peaks. Besides adhering particles at the peaks, the bare surface is visible with distinct solidification lines along the scan direction. In contrast, the ring-shaped beam profile with a power ratio of 20/80 produces considerably higher spherical, drop-shaped and cylindrical peaks, resulting in a higher surface roughness *Sa*. Additionally, almost no particles adhere to these peaks, but rather adhere to the valleys between the peaks, covering the solidification lines.

Compared to the up-skin surface, the side surface of the ring-shaped beam profile with a power ratio of 20/80 is also largely covered with particles, but exhibits shallower peaks. For the Gaussian beam profile, the side surface exhibit a dense coverage of attached particles. For this reason, no solidification lines are visible and the peaks are less pronounced compared to the up-skin surface. A layer pattern along the build direction is barely recognizable.

Discussion

The results reveal that the surface roughness depends on the surface orientation, the process parameters and the beam profile. In order to discuss the influence of the process parameters on the surface roughness in the following, first the surface roughness formation of the Gaussian beam profile and the ring-shaped beam profile with a power ratio of 20/80 is examined with respect to the surface orientations using etched cross-sectional images. Lastly, the preferred beam profile for each surface orientation is discussed.

Surface Roughness Formation of the Gaussian and Ring-Shaped Beam Profiles

In Figs. 14 and 16, etched cross-sectional images of the surfaces from Fig. 13 with the lowest surface roughness *Sa* for the Gaussian beam profile (Fig. 13a) and the ring-shaped beam profile with a power ratio of 20/80 (Fig. 13b) for all investigated surface orientations are shown. In Fig. 14 the down-skin surfaces and in Fig. 16 the up-skin and side surface are presented. Exemplary melt pool boundaries are highlighted. A solid line is used for the hatch, a dotted line for the contour 2 (inner contour) and a dashed line for the contour 1 (outer contour).

For all surface orientations, an at least five times deeper melt pool is observed for the Gaussian beam profile in Figs. 14a and 16a compared to the ring-shaped beam profile at a power ratio of 20/80 in Figs. 14b and 16b. In addition, a U-shaped melt pool geometry, which is characteristic for keyhole welding, is observed for the Gaussian beam profile, while the ring-shaped beam profile at a power ratio of 20/80 has a semicircular melt pool geometry, which is characteristic for heat conduction welding. This is consistent with the melt pool geometry of single-track experiments reported in the literature [30, 31].

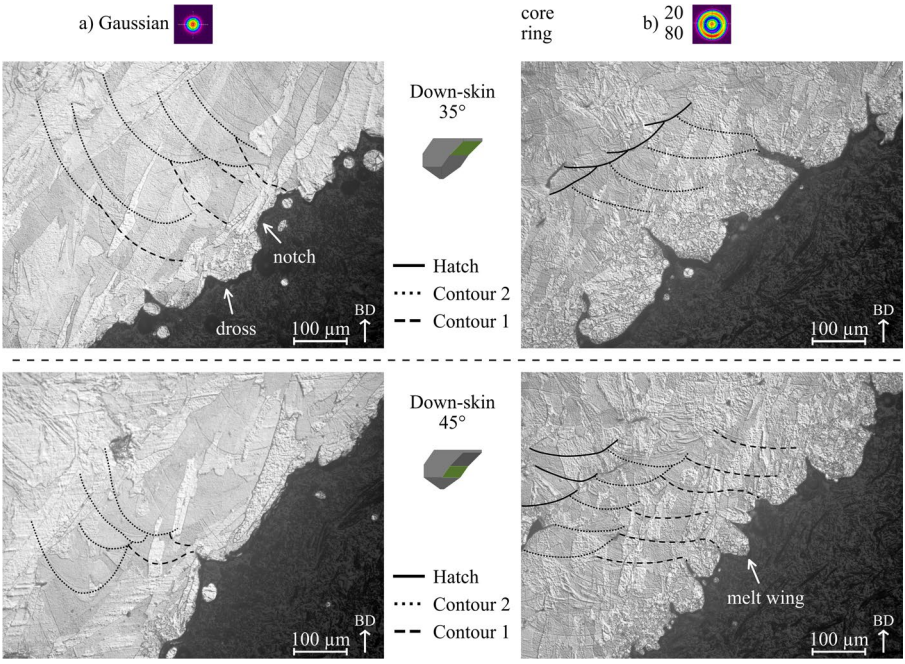

Fig. 14 Etched cross-sectional images of the down-skin surfaces at an inclination angle of 35° and 45° with the lowest surface roughness *Sa* from Fig. 13 using **a)** the Gaussian beam profile and **b)** the ring-shaped beam profile with a power ratio of 20/80

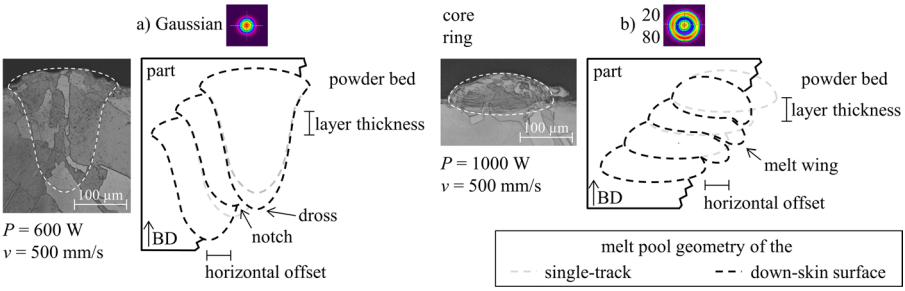

Fig. 15 Sketch of contour 1 of the down-skin surface at an inclination angle of 45° using **a**) a Gaussian beam profile and **b**) a ring-shaped beam profile with a power ratio of 20/80. The weld geometry is obtained from an etched cross-sectional image of a single-track welded with a laser power and scan speed according to the surface with the lowest surface roughness Sa in Fig. 13. The experimental procedure of the single-track experiments are described in the respective publication [30, 31]

The cross-sectional images of the down-skin surfaces at an inclination angle of 35° and 45° in Fig. 14a show that the melt pool of contour 2 is regular stacked on the previous solidified layer for the Gaussian beam profile. In contrast, the melt pool of contour 1 is only supported one-sided by the solidified material due to the horizontal offset of the previous layer caused by the inclination angle and thus penetrates the powder layer against the build direction, which is sketched in Fig. 15a. The weld

geometry is obtained from a etched cross-sectional image of a single-track produced at a similar laser power of 600 W and scan speed of 500 mm/s [31]. It should be noted that weld tracks of copper under process conditions are on average around 35 µm shallower compared to single-track experiments on substrate [31]. In addition, the numeric simulation of the contour exposure of overhanging structures of AlSi10Mg reveals that the melt pool is asymmetrical and extends more into the powder bed than into the solidified material [51]. However, a similarity with Fig. 14a is recognizable.

The part contour depends mainly on the shape of the melt pool facing the powder bed. In the case that the melt pool penetrates the powder bed further in one layer compared to the previous layer, the melt pool protrudes downwards into the powder bed and a dross form. In the opposite case that the melt pool protrudes the powder bed less than the previous and subsequent layer, a notch is formed.

Consequently, the surface roughness is formed by the tip of the melt pool and thus depends on the keyhole. A keyhole forms when the recoil pressure overcomes the pressure produced by the surface tension [52, 53]. Multi-reflection occurs in the keyhole, enabling energy transfer to its tip. Numerical simulations reveal that temperature variations on the melt pool surface as well as pressure fluctuations and vapor circulation occur within the keyhole, causing dynamic changes of the back wall of the keyhole [46, 53, 54]. In contrast, the angle of the front keyhole wall is rather constant [46]. The flow field in the melt pool contribute to the transient nature of the keyhole shape, causing the keyhole depth and radius to fluctuate [53]. The variability of the keyhole shape during keyhole welding is confirmed by in-situ high speed x-ray imaging using a Gaussian beam profile on a bare substrate of Ti6Al4V [54]. In addition, a powder layer of Ti6Al4V on top of the substrate tends to induce more fluctuation of the keyhole compared to the bare substrate [55]. The metal vapor jet cause the ejection of liquid droplets, as observed for Ti6Al4V both on a bare substrate and in case of a powder layer [41, 54]. Over a powder bed, the liquid droplets may fuse with the loose powder particles and form powder agglomeration spatter [41, 56]. Agglomeration spatter can exceed the particle size distribution of the powder, affecting the melt pool depth and stability [56]. In addition, the metal vapor flow induces an argon flow near the melt pool due to the Bernoulli effect. This either ejects adjacent powder particles from the powder bed or draws them into the melt pool, forming a denudation zone [57–59]. Ejected powder particles, known as entrainment melting spatter, may pass through the laser beam, partially absorbing the laser radiation and thus blocking the laser beam [41, 52, 56, 58]. Powder particles drawn into the melt pool at a lower temperature disturb the melt pool [52]. Therefore, the authors assume that fluctuations of the keyhole due to the melt pool dynamics, spatter and the powder bed homogeneity led to the variations in the melt pool depth.

As the inclination angle increases from 35° to 45°, the part contour consists of wider and shallower convex and concave areas with a rather smooth transition, shown in Fig. 14a, instead of sharp notches and bulges. The authors assume that this is the result of the decreased horizontal offset and increased vertical offset of the contour exposure between the layers, so that the tip of the melt pool is supported over a larger area by the underlying material and thus ensures a smoother interface even in case of fluctuations.

The down-skin surfaces at an inclination angle of 35° and 45° are entirely covered with particles apart from the valleys where the bare surface and some solidification lines of the melt pool are visible in Fig. 8. The authors assume that this is due to the dross and notch formation. In the case of a notch, the tip of the melt pool is located in the previously solidified layer and the denudation zone next the melt pool prevents particle attachment, forming a valley with recognizable solidification lines. In the case of a dross, the tip of the melt pool is located in the powder bed. Although a denudation zone is also present in this case, it does not extend below the tip of the melt pool. Consequently, the tip of the melt pool is surrounded by powder particles. For pure copper, the thermal conductivity λ decreases by one order of magnitude from around 412 to 0.4 W/(mK) for loose powder particles with a particle size of 40 µm compared to pure copper samples produced via PBF-LB/M [9, 10]. As the dross maintains a higher temperature over a longer period of time compared to the remaining part, particles may sinter to the dross or experienced partial melting.

For the down-skin surface at an inclination angle of 45° using the ring-shaped beam profile at a power ratio of 20/80 in Fig. 14b, regular stacked melt pools of contour 2 and contour 1 are visible. It is evident that contour 2 is completely supported by the previous layer, whereas contour 1 is only supported by the powder bed over the length of the horizontal offset, as sketched in Fig. 15b. The melt pool geometry is obtained from a etched cross-sectional image of a single-track produced at an identical laser power of 1000 W and scan speed of 500 mm/s [30]. Similar to the Gaussian beam profile, differences in the melt pool geometry between the process conditions and the etched cross-sectional image of a single-track are expected. However, a similarity with Fig. 14b is recognizable.

Compared to the Gaussian beam profile in Figs. 14a and 15a, the melt pool geometry of the ring-shaped beam profile in Figs. 14b and 15b is significantly shallower. As described in Sect. 1.3, ring-shaped beam profiles form a depression zone composed of a core depression and an annular depression corresponding to the intensity peaks of the intensity distribution, whereas the Gaussian beam profile forms a single depression in the center [36]. Although the laser power increases from 600 W for the Gaussian beam profile to 1000 W for the ring-shaped beam profile in Fig. 15, the peak intensity reduces from around 39 to 7 MW/cm² due to the beam diameter and intensity distribution, as shown in Fig. 4. For this reason, ring-shaped beam profiles tend to have a lower maximum temperature and temperature gradient in the melt pool compared to a Gaussian beam profile, reducing vaporization, inherent recoil pressure and melt pool velocity [35–37]. Consequently, the depth of the depression zone tends to decrease, enabling ring-shaped beam profiles to avoid keyhole formation, which is evident for the Gaussian beam profile in Figs. 14 and 15, even with increasing laser power [35, 39, 43]. It should be noted that the beam diameter $D_{4\sigma}$ increases from 62 µm for the Gaussian beam profile to 171 µm for the ring-shaped beam profile, prolonging the interaction time. A longer interaction time tends to increase the weld depth and weld width [31]. However, considering Fig. 15, this is less decisive for the weld width and depth compared to the peak intensity.

The highlighted melt pool boundaries in Fig. 14b and the cross-sectional image in Fig. 15b reveal an almost horizontal course of the weld seam in the solid material. However, the melt pool is located partially in the powder bed due to the horizontal

offset. As the melt pool in the powder bed is only supported by loose powder particles, the melt penetrates into the powder bed due to its own weight and gravity. The numerical simulation of single-tracks of Ti6Al4V using ring-shaped beam profiles reveals an increase in melt pool depth around the annular depression zone due to the recoil pressure, as well as an inwards and outwards flow induced by the Marangoni effect [36]. The etched cross-sectional image in Fig. 14b reveals a weld width of around 200 µm, which is in good agreement with the highlighted weld seam geometry in Fig. 15b. The intensity peaks of the ring-shaped beam profile with a power ratio of 20/80 are around 126 µm apart with a beam diameter $D_{4\sigma}$ of 171 µm, as shown in Fig. 4. As the weld width corresponds roughly to the intensity distribution, the authors assume that the outwards Marangoni flow and the annular depression zone enhances the penetration of the melt pool into the powder bed.

As the melt solidifies, the part of the melt pool in the powder bed solidifies as a downward-hanging melt wing. For this reason, the melt wings in Fig. 14b exhibit a regular interval corresponding to the layer thickness. The intensity images and three-dimensional representations of the down-skin surface at an inclination angle of 45° in Fig. 13c exhibit peaks and valleys, corresponding to the melt wings and the notches between them, respectively. From layer to layer, variations in the size of the melt wing as well as the shape and depth of the melt pool of contour 2 and contour 1 in the resolidified material are evident in Fig. 14b. The authors assume that fluctuations in the melt pool geometry occur due to the melt pool dynamics at the depressions as well as spatter and the powder bed, as described in detail for the Gaussian beam profile. However, ring-shaped beam profiles tend to less intense melt pool dynamics compared to a Gaussian beam profile, as there is less vaporization, inherent recoil pressure and melt pool velocity [35–37].

For the down-skin at an inclination angle of 35°, notches that extend to contour 2 are observed in the cross-sectional image. Although contour 1 is not visible due to the grains, assuming that contour 1 is at a similar position relative to contour 2 as for an inclination angle of 45°, it is evident that contour 1 irregularly aggregates over multiple layers. This leads to the higher peaks and deeper valleys observed in Fig. 13c for an inclination angle of 35° compared to an inclination angle of 45°, resulting in a higher surface roughness. In addition, the down-skin surfaces at an inclination angle of 35° and 45° are densely covered with particles. The cross-sectional images show that these particles attach primarily to the bottom side of the melt wing. Due to the lower thermal conductivity of the power bed compared to the solid material, a higher temperature is maintained over a longer period of time in the melt wing compared to the remaining part of the weld seam, enabling the sintering of particles to the melt wing [9, 10]. However, a denudation zone forms during welding [57–59]. The authors therefore assume that the denudation zone next to the melt track prevents powder attachment at the side, while powder particles below the melt wing sinter or partially melt at the bottom side of the melt wing due to the slow heat dissipation in the powder bed.

For the contour exposure of the up-skin and side surface, the melt pool form on the previously solidified layer and the heat is mainly conducted through the previously solidified layer, as shown in Fig. 1. The etched cross-sectional images of the up-skin at an inclination angle of 45° and side surface in Fig. 16 show that the melt pool of

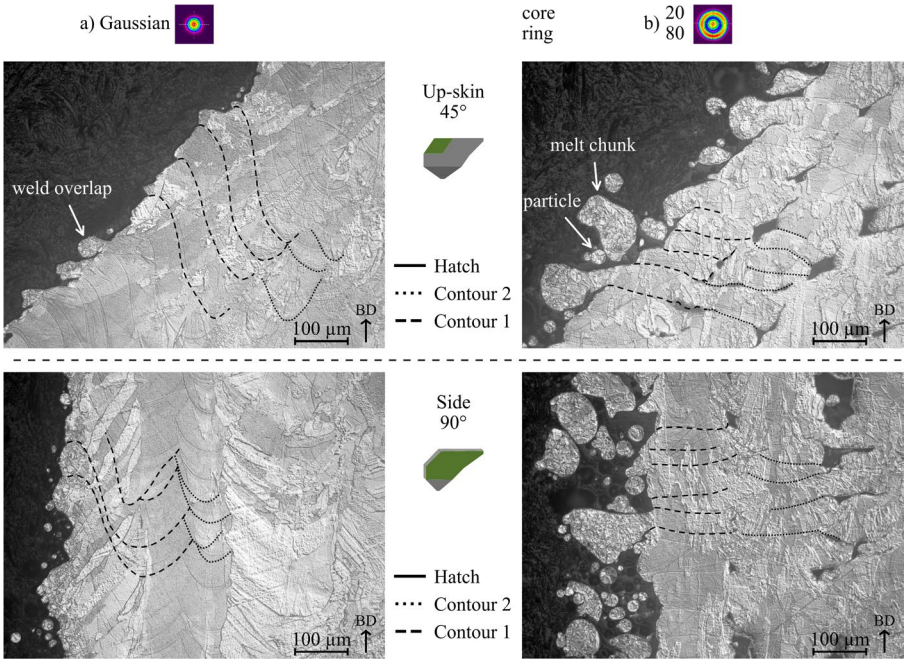

Fig. 16 Etched cross-sectional images of the up-skin surface at an inclination angle of 45° and the side surface with the lowest surface roughness *Sa* from Fig. 13 using **a**) the Gaussian beam profile and **b**) the ring-shaped beam profile with a power ratio of 20/80

contour 2 and contour 1 are regularly stacked on the previously solidified layer for both the Gaussian beam profile and the ring-shaped beam profile at a power ratio of 20/80.

For the Gaussian beam profile in Fig. 16a, the contour exposures remelt a large portion of the underlying layer. In contrast to the down-skin, the weld depth has no direct effect on the surface roughness of the up-skin and side surface. Instead, the staircase effect and the shape and width of the weld face contributes to the surface roughness. From layer to layer, variations in the shape of the weld face of contour 1 are evident. In addition, variations in weld width and depth are also noticeable, indicating fluctuations in melt pool dynamic at the depression, as described in detail for the down-skin surface [46, 53, 54, 56]. During cooling, the surface tension is the dominant force, shaping the weld face [34]. Due to the temperature gradient and the temperature depended surface tension coefficient, capillary, Marangoni and wetting forces contribute to the curvature of the surface [34, 46, 47]. In addition, buoyancy and gravity forces apply. Furthermore, vapor escaping the depression mixes with the ambient air and produces surface drag [46]. As these forces and the melt volume fluctuate along the scan direction, variations in the shape of weld face occur, which are documented in both numerical simulations and experiments [24, 34, 35, 46, 54, 56].

Weld overlap is observed for the up-skin surface, which occurs when the melt is pulled outwards due to the recoil pressure and Marangoni flow and has not enough time to combine with the weld face before solidifying. The weld overlap forms the

peaks on the surface in Fig. 13b. In addition, particles adhere to these peaks. The authors assume that the widespread absence of powder attachment to the surface in Fig. 13b is caused by the denudation zone, either pulling surrounding particles into the melt pool or ejecting them from the powder bed [57–59]. However, the overlapping melt tends to hang downwards due to its own weight and gravity, enabling contact with powder particles below or outside the denudation zone. Due to the lower thermal conductivity of the power bed compared to the solid material, a higher temperature is maintained over a longer period of time in the weld overlap, enabling the sintering or partially melting of particles to the weld overlap [9, 10].

Compared to the up-skin surface, the side surface is largely covered with particles, as shown in Fig. 13b, reducing the surface roughness due to less height differences. The cross-sectional image in Fig. 16a shows individual, unmolten particles on the surface, indicating that the particles are sintered to the part contour and to each other due to the local temperature. For the side surface, there is only material with a thickness of up to around 150 µm between the melt pool and the powder bed, while the material thickness increases to more than 350 µm for the up-skin surface. For this reason, the heat of the material between the melt pool and the powder bed of the side surface dissipates slower compared to the up-skin, so that a higher temperature is maintained over a longer period of time, enabling the sintering of particles to the subjacent layers.

For the ring-shaped beam profile in Fig. 16b, the etched cross-sectional images of the up-skin and side surface show that the spherical, drop-shaped or cylindrical peaks observed on the surface in Fig. 13c are protruding, solidified melt chunks, which exceed the particle size distribution and are only partially connected to the surface by a tapered stem. For the side surface, these melt chunks tend to protrude rather horizontally into the powder bed, whereas for the up-skin surface they tend to hang on the subjacent layers. In addition, particles attach to these melt chunks and the surface, forming the surface roughness.

In order to examine the formation of the melt chunks, two supplementary experiments conducted independently of each other are considered. In one experiment, a weld track welded onto a substrate with an applied powder layer of 90 µm, and in the other experiment, a weld track welded on top of a cubic sample, which is manufactured using a layer thickness of 45 µm [30]. The top view of the respective weld tracks, which are welded in both experiments with the same laser power of 1000 W and scan speed of 500 mm/s, are shown in Fig. 17a and b. Both weld tracks have a comparable weld width of around 180 µm, which is also in good agreement with the width of the contour exposure in Fig. 16b, although the steady state of the PBF-LB/M process is not necessarily present for the weld tracks welded onto the substrate. The weld tracks broaden noticeably in irregular intervals, exhibiting protruding material perpendicular to the scan direction with a length in the range of 132–144 µm. Depending on the width of the protruding material, a droplet, as observed in Fig. 17a, forms due to the surface tension. The authors assume that the protruding material are the melt chunks observed in Fig. 16b, as the size is comparable.

Variations in weld width along the scan direction are evident for both weld tracks. However, the weld track on top of the cubic samples in Fig. 17b exhibits larger and more frequent variations in weld width and a more frequent occurrence of melt chunks

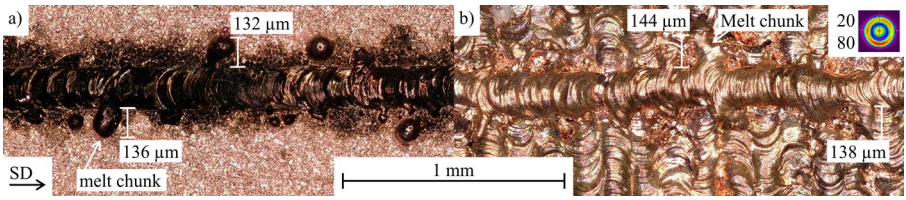

Fig. 17 Top view of weld tracks welded **a**) on a substrate plate with an applied powder layer of 90 µm and **b**) on the top surface of a cubic sample manufactured with a layer thickness of 45 µm using a ring-shaped beam profile at a power ratio of 20/80 with a laser power P of 1000 W and a scan speed v of 500 mm/s [30]. The experimental procedure of the single-track experiments is described in the publication [30]

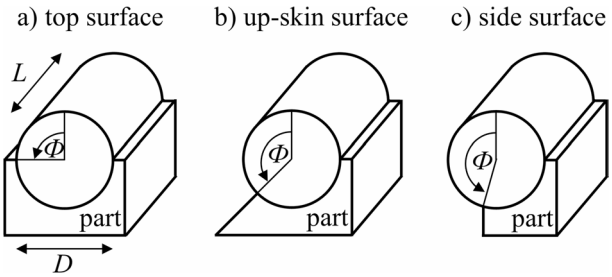

Fig. 18 Sketch of the segmented cylinder with diameter D, melt pool length L and the contact width specified by the angle Φ for **a**) the top surface, **b**) an up-skin surface and **c**) the side surface according to [60]

compared to the weld track on the substrate in Fig. 17a. The authors assume that this is related to the higher surface roughness of the top surface of the cubic sample compared to the substrate. Yadroitsev et al. describe the melt pool in the PBF-LB/M process as a segmental cylinder and define a stability criterion against disturbance

$$\frac{\pi\, D}{L} > \sqrt{2}\sqrt{\frac{\Phi\ (1+\cos 2\Phi\ ) - \sin 2\Phi}{2\Phi\ (2+\cos 2\Phi\ ) - 3\sin 2\Phi}} \tag{1}$$

with the diameter D, the melt pool length L and the contact width specified by the angle Φ, as sketched in Fig. 18, applicable at $\Phi > \pi/2$ [60]. The segmental cylinder is stable at any melt pool length if $\Phi < \pi/2$ [60]. For a given diameter and melt pool length, the local stability criterion may be violated if the angle Φ increases locally due to convex regions on the surface, whose curvature is higher for a rough surface than for a flat surface.

The stability criterion may also explain the increasing number of melt chunks observed from the top surface of the cubic sample in Fig. 17a over the up-skin surface to the side surface of the inclined cube geometry in Fig. 16b. The sketch in Fig. 18 illustrates that the angle Φ of the contact width increases from the top surface over the up-skin surface to the side surface. Consequently, for a given diameter and melt pool length, which depend on the process parameters, the margin to the stability limit

reduces or the stability criterion is even violated. The onset of weld track instability with increasing inclination angle is confirmed by single-tracks of AISI 316 L welded on the up-skin surface with an inclination angle in the range of 0° (top surface) to 70° [61]. Therefore, the contour exposure of the side surface is more susceptible to instability than the up-skin surface, followed by the weld track on top of the cubic sample and on the substrate.

Besides the geometric influence of the surface orientation and the surface roughness, the angle Φ is related to the melt pool depth [60]. During heat conduction welding, the laser beam vaporizes material, generating recoil pressure that forms the depression zone [34–36]. In addition, temperature gradients in the melt pool lead to a melt pool flow due to the Marangoni effect, contributing to the depression formation [34–36]. Consequently, fluctuations in the melt pool dynamics and energy input due to splatter or powder bed inhomogeneities, as previously described, effect the depression and thus the melt pool length, depth and width [41, 56]. The melt chunks therefore form due to weld track instabilities resulting from a combination of the surface orientation, the roughness of the underlying layer, and process-related fluctuations in the melt pool geometry. This is consistent with a study of the side surface roughness of AlSi10Mg and Inconel 718 tubes, which observed spherical features with around 100 µm in size due to melt pool instability [48]. However, further experiments or numerical simulations are necessary to determine the respective influence of surface orientation, roughness of the underlying layer, and process-related fluctuations in the melt pool geometry on the weld track instability.

Since the angle Φ approaches the maximum for the down-skin surface, the authors assume that some of the changes in size and shape of the melt wings from layer to layer in Fig. 14b are also caused by instabilities.

Surprisingly, the measured surface roughness of the side surface is lower than the surface roughness of the up-skin surface, although the cross-sectional images show more powder attachment and melt chunks on the surface. The authors assume that this can be explained by the optical surface roughness measurement. The powder particles fill the gap between the melt chunks so that the actual surface of the resolidified contour 1 exposure is covered. For that reason, a lower surface roughness is measured for the side surface compared to the up-skin surface, where less powder particles adhere and therefore the melt chunks protrude clearly from the actual surface.

The cross-sectional images for the ring-shaped beam profile at a power ratio of 20/80 in Figs. 14b and 16b reveal that the appropriate offset to avoid contour porosity depends on the surface orientation. For the down-skin surface at an inclination angle of 35° and 45°, no contour porosity is observed, but for the up-skin surface and the side surface, although the offsets are identical. However, the authors assume that the contour porosity has no influence on the measured surface roughness, as the surface roughness is formed by the protruding melt chunks and the attached particles. The authors expect that these are also present with a reduced offset between the hatch and the contour exposures, which avoids contour porosity. In addition, investigations on the magnesium alloy WE43 have shown that contour porosity tends to have no significant influence on the surface roughness using two contour exposures [18].

Influence of the Process Parameters on the Surface Roughness and Surface Characteristics Using a Gaussian Beam Profile

For the down-skin surface, the surface roughness is formed by the downwards penetration of the powder bed by the tip of the melt pool, as shown in Fig. 14a. Therefore, the surface roughness depends on the width and depth as well as stability of the keyhole. The depth of the keyhole tends to increase with increasing laser power or decreasing scan speed and is linearly related to the tangent of the front keyhole wall angle [55]. While the angle of the front keyhole wall is rather constant, the keyhole back wall exhibit a highly dynamic oscillation, causing fluctuations in the depth and radius of the keyhole [46, 53].

In the PBF-LB/M of copper at a laser power of 400 and 500 W, the weld width of single-tracks of copper tends to decrease with increasing scan speed from 50 to 500 mm/s [62]. A decreasing trend of the weld width and depth is also evident with increasing scan speed from 100 to 1000 mm/s, whereas the weld width and depth tends to increase with rising laser power from 300 to 500 W [23]. A similar trend is observed with increasing laser power up to 1000 W [31]. Furthermore, weld track instability emerge with decreasing laser power in the range of 500–1000 W or increasing scan speed in the range of 100–800 mm/s [63].

As the weld depth and width decrease with an increasing scan speed and thus the melt pool penetrates less into the powder bed, a decrease of the down-skin surface roughness $\overline{Sa}$ is expected. However, the main effect diagram in Fig. 7b reveals an increase in surface roughness with an increasing scan speed from 400 to 600 mm/s followed by a reduction in surface roughness as the scan speed rises up to 800 mm/s. The authors assume that at a scan speed of 400 mm/s a rather stable keyhole exists, resulting in a deep melt pool with minimal fluctuations along the scan direction and from layer to layer. As the scan speed increases to 600 mm/s, fluctuations of the melt pool intensify, and keyhole instabilities occur more frequently, resulting in deeper valleys on the part surface as the keyhole collapse and higher peaks due to the melt pool depth with a formed keyhole, as shown in Fig. 8. A further increase in scan speed to 800 mm/s decreases the keyhole depth [31], reducing the spread between the weld depth with a formed keyhole and a collapsed keyhole. Therefore, the spread between the peaks and valleys decreases and a rather uniform surface is formed, resulting in a reduction of the surface roughness $\overline{Sa}$. This is particularly noticeable for a laser power of 1000 W by a decrease in the height of the peaks and depth of the valleys in Fig. 8 as the scan speed decrease from 600 to 800 mm/s.

At a scan speed of 500 mm/s, the weld depth increases considerably from around 140 to 460 µm with an increasing laser power from 500 to 1000 W for a Gaussian beam profile with a comparable beam diameter of 62 µm [31]. However, the main effect diagram in Fig. 7a shows almost no effect of the laser power in the range of 500–1000 W on the surface roughness $\overline{Sa}$ for the down-skin surface at an inclination angle of 35° and 45°. In addition, only slight differences in the height of the peaks and the number of attached particles are visible in Fig. 8 with increasing laser power from 500 to 1000 W for all scan speeds. In contrast, the scan speed has a pronounce effect in the investigated parameter range, indicating that variations of the weld depth caused by keyhole instabilities are more decisive than the weld depth.

The cross-sectional images in Fig. 16a indicate that the surface roughness of the up-skin and side surface is formed by the weld face shape and weld overlap. Under ideal conditions, the weld face forms a semi-circular face due to the surface tension, so that the weld face is defined by its width and height. However, fluctuations in capillary, Marangoni and wetting forces in combination with surface drag produced by escaping vapor lead to deviations from this ideal shape of the weld face and weld overlap along the scan direction [34, 46, 47]. As melt pool instabilities tend to emerge with a decreasing laser power or an increasing scan speed [63], the authors expect a decrease in the up-skin and side surface roughness with an increasing laser power and a decreasing scan speed. This is consistent with the trend lines of the main effect diagram of the up-skin and side surface roughness $\overline{Sa}$ in Fig. 7.

Considering the surface characteristics in Fig. 8, the number of sintered particles on the up-skin and side surface increases with rising laser power from 500 to 1000 W. The authors assume that the temperature field spread further into the material as the laser power rises. Since the sintering activity of particles tends to increase with rising temperature or dwell time, the number of sintered or partially molten particles is expected to rise with an increasing laser power. These particles fill the gaps between the peaks, forming large-area peaks and thus reducing the surface roughness $\overline{Sa}$ in Fig. 7a.

In contrast, Fig. 8 reveals an increase in the number and height of the peaks on the surface with increasing scan speed from 400 to 800 mm/s, raising the surface roughness $\overline{Sa}$ in Fig. 7b. Therefore, shape deviations of the weld face and weld overlap increase, indicating rising fluctuations in capillary, Marangoni and wetting forces as well as surface drag and thus a less stable welding process. This is consistent with investigations on the side surface roughness of tubes made of Inconel 718 and AlSi10Mg, which point out an increase in surface roughness *Sa* and *Sv* with an unstable contour melting [48].

Comparing the effect of the laser power and scan speed on the surface roughness in Fig. 7, it is evident that the scan speed has also a more pronounced effect on the up-skin and side surface roughness than the laser power in the investigated parameter range. Therefore, the stability of the melt pool is also the more decisive factor for the up-skin and side surface.

Influence of the Power Ratio and the Process Parameters on the Surface Roughness and Surface Characteristics Using Ring-Shaped Beam Profiles

Changing the power ratio from 35/65 to 20/80 or 10/90 at similar laser power tends to reduce the peak intensity in the center of the laser beam, as shown in Fig. 4, decreasing the recoil pressure in the center. Single-tracks produced with a laser power of 1300 W and a scan speed of 400 mm/s reveal that the weld width decreases from around 300 to 230 µm and the weld depth from around 180 to 30 µm as the power ratio changes from 35/65 to 20/80 or 10/90, whereby the power ratio of 20/80 and 10/90 have a similar weld width and weld depth [30]. In addition, the aspect ratios of the single-tracks, given by the weld depth divided by the weld width, indicates a heat conduction welding process ($R < 0.5$) for a power ratio of 20/80 and 10/90, whereas keyhole formation ($R \geq 0.5$) is observed for a power ratio of 35/65 [30]. As the surface

characteristics in Fig. 9b-d and the weld width, weld depth as well as welding regime of the ring-shaped beam profiles with a power ratio of 20/80 and 10/90 are comparable, the authors assume a similar surface roughness formation as shown in Figs. 14b and 16b. In contrast, for the power ratio of 35/65 the aspect ratios of single-tracks reveal keyhole formation, which is linked to the onset of multi-reflection of the laser beam [30, 32]. Numeric simulations of single-tracks welded on a AISI 316 L plate show that the melt pool length and depth as well as the flow dynamic and surface morphology of a Gaussian beam profile and a ring-shaped beam profile with a power ratio of 40/60 are identical for a similar beam diameter of 107 µm and laser power of 300 W due to multi-reflection [47]. Despite the minor difference in power ratio, the authors therefore assume that the ring-shaped beam profile with a power ratio of 35/65 is rather comparable to a Gaussian beam profile of a similar beam diameter and laser power. It is crucial to note that the beam diameter of the investigated Gaussian beam profile is around 2.5 times smaller than the beam diameter of the ring-shaped beam profile with a power ratio of 35/65 (see Table 3), thus no comparison with the Gaussian beam profile used in this study based on similar process parameter is feasible.

Nevertheless, the authors assume that a transition of the surface roughness formation explain the main effect diagram in Fig. 9a. As the surface roughness formation of the down-skin surfaces transition from the downwards penetration of the powder bed by the tip of the weld seam towards an unsupported melt wing hanging downwards into the powder bed as shown in Fig. 14 when the power ratio changes from 35/65 to 20/80 or 10/90, the height of the peaks and depth of the valleys reduces, decreasing the surface roughness $\overline{Sa}$. In contrast, for the up-skin and side surface the surface roughness formation transitions from weld overlap to protruding, solidified melt chunks that are only partially connected to the surface as shown in Fig. 16, which increases the surface roughness $\overline{Sa}$.

Furthermore, the authors assume that the transition of the surface roughness formation is related to the transition of the welding regime from heat conduction welding to keyhole formation, which occurs for an aspect ratio of $R \geq 0.5$ of the melt pool due to the onset of multi-reflection [30–32]. For the power ratios of 20/80 and 10/90, the aspect ratio of single-tracks is $R < 0.3$ for a laser power in the range of 1000–1300 W and a scan speed in the range of 400–900 mm/s [30]. Consequently, the welding regime does not change in the investigated parameter range and the surface characteristics remain almost unchanged, as evident in Fig. 12 for a power ratio of 20/80 and discussed later. In contrast for a power ratio of 35/65, the aspect ratio of single-tracks show keyhole formation at a laser power of more than 1000 W and a scan speed below 500 mm/s [30].

Considering the intensity images and three-dimensional representations of the up-skin surface at an inclination angle of 45° in Fig. 10, a change in surface characteristics occurs either with an increase in laser power from 1200 to 1300 W at a constant scan speed of 400 mm/s, or with a decrease in scan speed from 500 to 400 mm/s at a constant laser power of 1300 W. This is also evident for the side surface. For the down-skin surface at an inclination angle of 35° and 45°, the change occurs with an increase in laser power from 1200 to 1300 W at a scan speed of 400 mm/s, or with a decrease in scan speed from 600 to 400 mm/s at a laser power of 1300 W. Therefore,

for a laser power below 1300 W and a scan speed above 400 mm/s, the surface characteristics of all the investigated power ratios are similar.

Comparing the observed threshold with the threshold of laser power and scan speed for keyhole formation reported for single-tracks, it is in good agreement for the scan speed [30]. However, the observed threshold for the laser power is higher than the laser power of more than 1000 W reported for the single-tracks [30]. The authors assume that this is caused by differences in the process conditions between the steady state of the PBF-LB/M process and the single-tracks on substrate experiment in the literature [30].

Process-induced preheating occurs depending on the volume energy density and the inter layer time [64]. For an interlayer time of 116 s and a volumetric energy density of around 82 J/mm³, which is closest to our experiments, the temperature on top of the sample measured by in-situ infrared thermography increases from the preheating temperature of 100 °C to around 180 °C [64]. Furthermore, an increase in build plate temperature from room temperature to 108 °C during manufacturing of cubic samples with a height of 10 mm of copper using a Gaussian beam profile with a beam diameter of 62 µm is reported [31]. For a laser power in the range of 600 to 900 W, a scan speed of 500 mm/s and a beam diameter of 88 µm the weld width, weld depth and aspect ratio increase by 7%, 22%and 1%, respctively, when the preheating temperature rise from room temperature to 100 °C [31]. Consequently, the laser power required for keyhole formation is reduced due to the process-induced preheating.

In contrast, in-situ laser profilometry found an effective powder layer thickness with a mean value in the range of around 60 to 120 µm for a nominal layer thickness of 30 µm during the processing of AlSi10Mg [13]. This is consistent with the effective powder layer thickness of around 200 µm measured by in-situ thermography for a nominal layer thickness of 50 µm during the processing of AISI 304 L [65]. Therefore, a powder layer of 90 to 180 µm is expected in the steady state of the PBF-LB/M process for a nominal layer thickness of 45 µm used in this study, which is at least as thick as the powder layer of 90 µm used for the single-track experiment [30]. The numerical simulation of single-tracks of H13 tool steel using a Gaussian beam profile with a laser power of 200 W and a scan speed of 1000 mm/s reveal a constant melt pool geometry with increasing layer thickness from 30 to 100 µm [66]. However, the weld width, weld depth and aspect ratio measured at the substrate surface decrease by around 40%, 54% and 24, resectively with increasing layer thickness from 30 to 70 µm [66]. For a layer thickness of 100 µm no penetration of the substrate is observed [66]. This is in good agreement with a single-track experiment using Ti6Al4V, which reveal a reduction in the weld width, depth, and aspect ratio by around 15%, 48%, and 25%, respctivey, when te layer thickness doubles from 20 to 40 µm [67]. As the powder layer thickness increases, more energy is required to completely melt the powder layer and achieve a similar weld depth and aspect ratio in the substrate.

Keyhole formation due to multi reflection starts at an aspect ratio of $R = 0.5$ [32]. Assuming that process-induced preheating raises the surface temperature to 100 °C and that the powder layer thickness doubles to 180 µm in the steady state of the PBF-LB/M process, the aspect ratio is reduced by a total of 12% to $R = 0.44$. For a ring-shaped beam profile with a power ratio of 35/65 and a scan speed of 400 mm/s,

the aspect ratio increases by 0.0313 for every 100 W in the heat conduction welding regime ($R<0.5$) with a coefficient of determination of $R^2 = 0.85$. An overview of the corresponding weld geometry based on single-track experiments with an applied powder layer of 90 µm is given in Fig. 19 in the appendix [30]. Consequently, the laser power required for keyhole formation increases by around 200 W, which is in good agreement with the observed difference to the single-track experiment. This strengthens the hypothesis of the authors that the change in surface characteristics is related to the transition from heat conduction welding to keyhole formation.

For the up-skin surface at an inclination angle of 45° in Fig. 10, a notable decrease in the number of attached particles as well as peaks, which are the melt chunks observed in Fig. 16b, is evident at the transition from heat conduction welding to keyhole formation. The authors assume that the number of attached particles decreases due to the increase in recoil pressure. With increasing recoil pressure, the induced argon flow near the melt pool intensifies [59]. As a result, the denudation zone expands, and less powder attach to the surface. Considering the number of melt chunks on the surface, the authors assume this is related to the weld track stability. For an aspect ratio of $R \geq 0.5$ on the top surface, the angle of the contact width corresponds to $\Phi \leq \pi/2$, whereas the angle of the contact width is $\Phi > \pi/2$ for an aspect ratio of $R<0.5$ [60]. Consequently, the angle of the contact width Φ is always lower for an aspect ratio of $R \geq 0.5$ than for an aspect ratio of $R<0.5$. Therefore, the welded track with an aspect ratio of $R \geq 0.5$ has a larger margin to the stability limit compared to the weld track with an aspect ratio of $R<0.5$. The weld track with a given diameter and melt pool length is thus more robust against the roughness of the underlying layer and process-related fluctuations in the melt pool geometry, resulting in fewer melt chunks on the surface.

A decline in the number of peaks and attached particles is also found for the side surface at the transition from heat conduction welding to keyhole formation, although almost half of the surface remains covered with particles in contrast to the up-skin surface due to the slower heat dissipation, as described in Chap. 4.1.

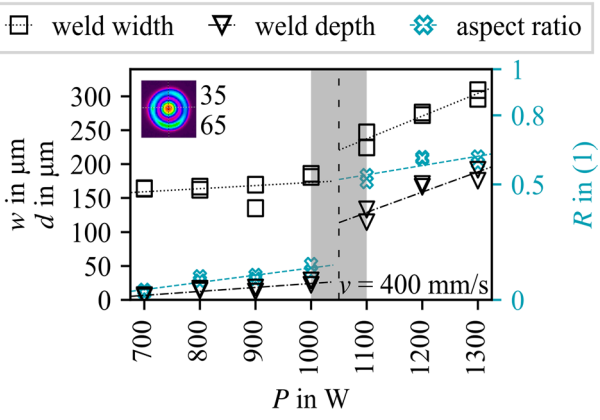

Fig. 19 Diagram of weld width w, weld depth d and aspect ratio R as a function of laser power P at a scan speed v of 400 mm/s using a ring-shaped beam profile with a power ratio of 35/65 [30]. The experimental procedure is described in the publication [30]

For the down-skin surface at an inclination angle of 35° and 45°, the transition from heat conduction welding to keyhole formation is less clearly visible. The most prominent change in surface characteristics is the reduction in particle attachment, which enhances the visibility of broader peaks and valleys, while height and depth remain almost unchanged at the transition. As previously stated, the authors assume that the denudation zone enlarges, reducing the number of attached particles. A rather constant height and depth of the peaks indicates that the transition from the melt wing hanging downwards into the powder bed to the penetration of the powder bed is occurring gradually.

Overall, a transition of the surface characteristics only occurs for a power ratio of 35/65 at a laser power above 1200 W and a scan speed below 500 mm/s, so that all but one of the parameter combinations investigated using a ring-shaped beam profile have similar surface characteristics. However, with varying laser power and scan speed, differences in the height of the peaks, the depth of the valleys and the number of attached particles on the surface are still observable in Fig. 12, which shows the ring-shaped beam profile with a power ratio of 20/80 as an example.

For single-tracks of pure copper, the laser power in the range of 1000–1300 W has almost no influence on the homogeneity of the weld tracks for a scan speed in the range of 400–900 mm/s [30]. In contrast, a scan speed in the range of 400–900 mm/s has an influence on the weld track homogeneity, indicating emerging process-related fluctuations in the melt pool with increasing scan speed [30].

For the down-skin surface at an inclination angle of 35° and 45°, the contour exposure consists of regular stacked melt pools and the surface roughness is formed by the unsupported melt wings, as shown in Fig. 14b. The authors assume that an increase in the melt pool width with increasing laser power from 1000 to 1300 W uniformly increases the size of the unsupported melt wings hanging downwards into the powder bed. Therefore, no changes in the height of the peaks or depth of the valleys are evident in Fig. 12. However, a slight enlargement of the areas free of attached particles is noticeable, which can be explained by an enlargement of the denudation zone with increasing laser power, leading to a slight decrease in surface roughness $\overline{Sa}$ in the main effect diagram in Fig. 11a. In contrast, Fig. 12 revels an increase in the height of the peaks and depth of the valleys with rising scan speed from 400 to 900 mm/s. Consequently, the authors assume that emerging process-related fluctuations in the melt pool enhance the variation of the melt wing size, increasing the surface roughness $\overline{Sa}$ with rising scan speed in the main effect diagram in Fig. 11b.

For the up-skin surface at an inclination angle of 45° and the side surface, the surface roughness $\overline{Sa}$ rises with an increasing laser power from 1000 to 1300 W, as shown in Fig. 11a. Considering the surface characteristics in Fig. 12, a slight increase in the height of the peaks for the up-skin surface and the side surface is evident. The authors assume, that the increased energy input enlarge the melt volume and thus the size of the melt chunks, increasing the surface roughness $\overline{Sa}$. As the scan speed increases from 400 to 900 mm/s, a slight increase in the height of the peaks is evident in Fig. 12. However, the main effect diagram in Fig. 11b shows almost no influence of the scan speed on the surface roughness, indicating that process-related fluctuations in the melt pool are less decisive for the formation of the melt chunks than the surface orientation and the roughness of the underlying layer.

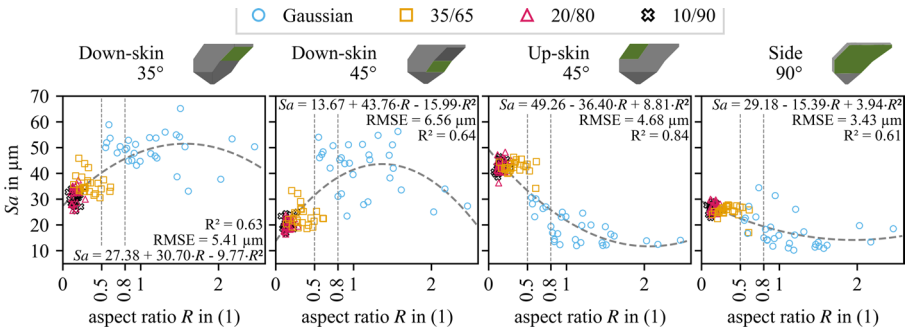

Fig. 20 Surface roughness *Sa* as a function of the mean aspect ratio *R* of single-tracks welded with identical laser power and scan speed as the respective contour exposure of the inclined cube geometry for a Gaussian beam profile [31] and the ring-shaped beam profiles with an power ratio of 35/65, 20/80 and 10/90 [30] for all investigated surface orientations. The experimental procedure and the results of the single-track experiments are described in the respective publication [30, 31]

Selection of the Beam Profile with Regards to the Surface Orientation

The previous findings indicate, that a change in the surface characteristic occurs with a change of the welding regime from heat conduction to keyhole formation, which can be identified by the aspect ratio *R* of the weld seam [31, 32].

In addition to the influence of process parameters such as laser power and scan speed, the aspect ratio of single-tracks increases for a Gaussian beam profile at a laser power of 700 W and scan speed of 500 mm/s from around 0.56 to 1.1 with decreasing beam diameter $D_{4\sigma}$ from 88 to 62 µm, due to an increase in peak intensity [31]. In contrast, at a similar peak intensity of 26 MW/cm², the aspect ratio decreases from 0.72 to 0.46 with a decreasing beam diameter from 88 to 62 µm, due to a decline in interaction time [31]. These findings are consistent with experimental results on single-tracks of AISI 304, which found a tendency for the aspect ratio to decrease when the laser beam is defocused due to a decrease in peak intensity despite an increase in beam diameter [50]. For ring-shaped beam profiles, an increase of the aspect ratio of single-tracks from around 0.17 to 0.49 is observed when the power ratio changes from 20/80 to 35/65 at a laser power of 1300 W, a scan speed of 500 mm/s and comparable beam diameters $D_{1.5}$ in the range of 164–166 µm [30]. An increase in the aspect ratio is also found in simulations of single-tracks of AlSi10Mg when changing the beam profile from a ring-shaped beam profile with a power ratio of 0/100 to a Gaussian beam profile of a similar beam diameter at an identical laser power and scan speed [35]. Consequently, the aspect ratio may function as a dimensionless number to compare disparate PBF-LB/M manufacturing configurations. In addition to material properties such as the absorption coefficient, the aspect ratio of the weld seam is determined by the process parameters such as laser power and scan speed, as well as the optical configuration and laser system, which defines the beam diameter and beam profile [23, 30–32, 35, 39, 42, 50, 67].

In Fig. 20, the measured surface roughness *Sa* is plotted as a function of the mean aspect ratio *R* of single-tracks produced with identical laser power and scan speed as the respective contour exposure for all investigated beam profiles [30, 31]. The

experimental procedure and the results of the single-track experiments are described in the respective publication [30, 31]. In order to conclusively determine the effect of the aspect ratio of the weld seam on the surface roughness, further experiments are necessary to increase the overlap of the aspect ratio R in the range of 0.5–0.8 and populate the range above 1.6 more densely. Furthermore, the authors discuss in the previous Sect. 4.3 that the process conditions of single-tracks on substrate and during the PBF-LB/M process may differ. However, the authors assume that a relative comparison is feasible, as the single-tracks and inclined cube geometries are each manufactured under similar process conditions.

For all investigated surface orientations, a relationship between the surface roughness of the inclined cubes and the aspect ratio of the single-tracks, welded with identical laser power and scan speed as the respective contour exposure, is found with a coefficient of determination R^2 in the range of 0.61–0.84 and a root mean square error (RMSE) in the range of 3.43–6.56 µm, as shown in Fig. 20. All regression coefficients have a p-value of 0.00, indicating significance. Utilizing the Q-Q plot of the different surface orientations with a confidence interval of 95%, only the side surface exhibits three data points that deviate significantly from a normal distribution. The presence of a cluster in the residual versus predicted plot indicates heteroscedasticity and a value in the range of 1.2–1.6 of the Durbin-Watson test indicates a slight positive autocorrelation of the different surface orientations. For that reason, ordinary least squares (OLS) with a robust standard error (HC3) is employed for the multiple linear regression. The quadratic model is selected for the up-skin and side surface, as a steep decline is evident for an aspect ratio in the range of 0.3–1, which flattens out above an aspect ratio of 1. For the down-skin surfaces, both a linear and a quadratic model are applicable. However, a comparison of the parameters R^2, adj. R^2, and RMSE reveals a substantial enhancement in the quadratic model. In contrast, higher-order polynomial models demonstrate negligible improvement, with the presence of non-significant factors. This is also apparent for the up-skin and side surface. The incorporation of additional process parameters into the model results in multicollinearity, given that the aspect ratio is inherently determined by laser power, scan speed, beam diameter and beam profile [23, 30–32, 35, 39, 42, 50, 67]. One potential modification to the model is the consideration of process instability, which might account for the observed scatter. According to the stability criterion (see Eq. 1), the length of the melt pool may be a suitable factor. However, there is a lack of data under similar process conditions, which must be generated using either high-speed imaging or numerical simulation.

For the down-skin surface at an inclination angle of 35° and 45°, the trend line indicates an increase in surface roughness Sa with increasing aspect ratio, peaking at around 1.6 and 1.4, respectively, and subsequently decreasing. It should be noted that the number of data points available for an aspect ratio $R > 1.5$ is limited to seven, Consequently, the reliability of this segment of the trend line is questionable. Given the reversal of the trend line, additional data points are required to support this segment. For this reason, the authors have decided against providing an interpretation. A considerable scattering of the data points from the trend line is evident for both down-skin surfaces, explaining the coefficient of determination R^2 in the range of 0.63–0.64. For a keyhole welding process $R \geq 0.8$, the surface roughness is formed

by the melt tip penetrating the powder bed, as shown in Fig. 14a. Decreasing the laser power, increasing the scan speed, decreasing the beam diameter or changing the beam profile from a Gaussian beam profile to a ring-shaped beam profile tends to reduce the aspect ratio, decrease the depth of the weld seam and thus the penetration of the powder bed [30, 31, 35]. For that reason, the surface roughness formation is transitioning towards the melt wing hanging downwards into the powder bed shown in Fig. 14b for an aspect ratio of around 0.13. Consequently, the use of ring-shaped beam profiles for the down-skin surfaces leads to a lower surface roughness *Sa* compared to the Gaussian beam profile in the investigated parameter range. Although aspect ratios of the single-track of $R<0.5$ are also attainable using the Gaussian beam profile, keyhole formation $R\geq0.5$ is necessary to achieve a continuous weld seam using a Gaussian beam profile with a beam diameter of 62 µm [31]. Therefore, the authors assume that the lowest achievable surface roughness is constrained, as occasionally broken or discontinuous weld tracks are likely to increase the surface roughness *Sa*. In contrast, ring-shaped beam profiles produce continuous weld tracks even for aspect ratios of $R\leq0.13$ and weld depths of less than 15 µm [30]. For that reason, ring-shaped beam profiles are suitable to reduce the surface roughness *Sa* of the down-skin surfaces.

For the up-skin and side surface, the trend line indicates a decrease in surface roughness *Sa* with increasing aspect ratio. This agrees with a study on the side surface roughness of tubes made of Inconel 718 and AlSi10Mg, which shows that the surface roughness tends to decreases as the melt pool transitions from conduction welding to keyhole welding for a Gaussian beam profile [48]. A considerable scattering of the data points from the trend line is evident for the up-skin and side surface. However, the coefficient of determination R^2 is larger for the up-skin surface compared to the side surface. The etched cross-sectional images in Fig. 14 reveal that the surface roughness is formed by the weld face accompanied by the staircase effect. In addition, weld overlap contributes to the surface roughness for the Gaussian beam profile, whereas melt chunks are observed for the ring-shaped beam profiles. As the melt chunks in Fig. 14b have a higher volume and number compared to the weld overlap in Fig. 14a, the Gaussian beam profile achieves a lower surface roughness *Sa* than the ring-shaped beam profiles. This findings is consistent with a study on cubic samples made of Inconel 718, which demonstrates an increase of the average side surface roughness *Sa* from around 11.32 to 11.62 µm when using a ring-shaped beam profile with an power ratio of 10/90 instead a Gaussian beam profile with the same volume energy density [45].

The minimum surface roughness *Sa* of the up-skin and side surface is achieved using a Gaussian beam profile at an aspect ratio of around 1.1 and thus in the keyhole welding regime. During keyhole welding, keyhole instability may cause keyhole pores within the resolidified material. In-situ high-speed x-ray imaging reveal that the use of a ring-shaped beam profile with a power ratio of 10/90 successfully eliminates keyhole pore formation during keyhole welding of a 100 µm thick powder layer of Ti6Al4V at a laser power of 550 W and a scan speed of 400 mm/s, due to the stabilization of the keyhole [54]. The authors therefore expect that ring-shaped beam profiles are capable of producing up-skin surfaces and side surfaces with a surface roughness comparable to the Gaussian beam profile, provided that a keyhole welding

process $R > 0.8$ is realized. In addition, near-surface porosity may be reduced due to the elimination of keyhole pore formation, enhancing component quality. However, the investigated laser power of 1300 W is not sufficient to enable keyhole welding using a ring-shaped beam profile with a power ratio of 20/80 or 10/90 [30]. Therefore, further research with a laser power of more than 1300 W is required.

Comparing the surface roughness measured in this study with the literature in Table 4 in the Appendix, the surface roughness *Sa* of the up-skin and side surface of around 10 and 12 µm respectively using a Gaussian beam profile is in the lower range of the literature, which ranges from around 12–20 µm. For the down-skin surface at an inclination angle of 45°, the ring-shaped beam profiles with a power ratio of 20/80 and 10/90 achieve a surface roughness *Sa* of around 17 µm, which is lower than reported in the literature using laser radiation in the green spectrum and near infrared spectrum with a surface roughness *Ra* in the range of 19–26 µm. However, for an inclination angle of 35° and below, the ring-shaped beam profiles achieve a surface roughness *Sa* of around 26 µm, which is only lower compared to studies using laser radiation in the near infrared spectrum. In contrast, the surface roughness *Sq* of the ring-shaped beam profile is higher than the study using laser radiation in the green spectrum.

Conclusion and Outlook

In this study, the use of Gaussian and ring-shaped beam profiles for the contour exposure of inclined cube geometries in the PBF-LB/M of pure copper are investigated. The influence of the process parameters on the surface roughness *Sa* and surface characteristics are studied for four different surface orientations such as down-skin surfaces at an inclination angle of 35° and 45°, an up-skin surface at an inclination angle of 45° and a vertical side surface. The lowest achievable surface roughness and respective surface characteristic of the different beam profiles are compared and the surface roughness formation is analyzed using etched cross-sectional images.

For the Gaussian beam profile, the main effect analysis show that the scan speed has a more pronounce effect on the surface roughness $\overline{Sa}$ compared to the laser power for all investigated surface orientations. Increasing the scan speeds tends to increase the surface roughness $\overline{Sa}$ due to melt pool instabilities. This is also evident for the investigated down-skin surfaces using ring-shaped beam profiles. In contrast, for the investigated up-skin and side surface the laser power has a more pronounce effect on the surface roughness $\overline{Sa}$ compared to the scan speed. With varying laser power and scan speed, differences in the height of the peaks and the depth of the valleys as well as the number of attached particles are observed for all investigated beam profiles.

A distinct difference in surface characteristics exists between the Gaussian beam profile and the ring-shaped beam profiles, whereas the surface characteristics of the ring-shaped beam profiles for all investigated power ratios are similar. An exception is the process parameter combination of a laser power of 1300 W and a scan speed of 400 mm/s, exhibiting a distinct change in surface characteristics between the power ratios of 35/65 compared to 20/80 and 10/90. The authors attribute this to the tran-

sition of the welding regime, identified by the aspect ratio of the weld seam, from conduction welding to keyhole formation.

The beam profile achieving the lowest surface roughness *Sa* in the investigated parameter range depends on the surface orientation. For the down-skin surfaces at an inclination angle of 35° and 45°, the ring-shaped beam profile with a power ratio of 10/90 achieves the lowest surface roughness *Sa* of around 25 and 16 µm compared to the Gaussian beam profile with a surface roughness *Sa* of around 33 and 23 µm. In contrast, for the up-skin and side surface, the Gaussian beam profile achieves the lowest surface roughness *Sa* of 12 and 10 µm compared to the investigated ring-shaped beam profiles with a surface roughness of up to 39 and 24 µm.

The surface roughness formation differs between the Gaussian beam profile and the ring-shaped beam profile. For the Gaussian beam profile, the surface roughness of the down-skin surfaces is formed by the melt tip penetrating the powder bed. In contrast, the surface roughness of the ring-shaped beam profile is formed by an unsupported melt wing hanging downwards into the powder bed, resulting in a lower surface roughness *Sa* compared to the Gaussian beam profile. For the up-skin and side surface, the surface roughness is formed by the weld face for both the Gaussian beam profile and the ring-shaped beam profile. However, for the Gaussian beam profile weld overlap is observed, whereas protruding, solidified melt chunks are evident for the ring-shaped beam profile, which results in a higher surface roughness *Sa* compared to the Gaussian beam profile.

For all investigated surface orientations, a trend between the surface roughness *Sa* of the inclined cube geometry and the aspect ratio of single-tracks, welded with identical laser power and scan speed as the respective contour exposure, is evident. For the investigated down-skin surfaces, the surface roughness *Sa* tends to increase with increasing aspect ratio up to an aspect ratio of 1.5, whereas for the up-skin and side surface the surface roughness *Sa* tends to decrease with increasing aspect ratio.

This study reveals that ring-shaped beam profiles achieve a lower surface roughness *Sa* of the down-skin surfaces compared to the Gaussian beam profile, by avoiding keyhole formation. In contrast, the keyhole welding process using the Gaussian beam profile achieves a lower surface roughness *Sa* of the up-skin and side surface compared to the heat conduction welding process using the ring-shaped beam profiles. However, ring-shaped beam profiles demonstrate the capability to stabilize the keyhole welding process and thus avoid keyhole porosity. The authors therefore expect that ring-shaped beam profiles are capable of producing up-skin surface and side surfaces with a comparable or even lower surface roughness than the Gaussian beam profile, provided that a keyhole welding process is realized. Therefore, further research with a laser power larger than 1300 W is necessary, which also increases the overlap of the aspect ratios. In addition, extending the investigation to other materials could validate the general applicability of these findings and minimize the surface roughness across various materials.

Appendix

Table 4 Overview of the lowest measured surface roughness of pure copper samples using laser radiation in the green and near-infrared spectrum for similar surface orientations from the literature and this study

Ref.	Wavelength	Beam	#	Parameter	Downskin		Side	Up-skin	Top
	in nm	profile	Contour	in µm	**25° −35°**	**45°**	**90°**	**45°**	
[5]	515	Gauss	n.m.	*Sq*	24.6–26.51	24.96		29.6	
[9]	515	Gauss	n.m.	*Ra*			19–20		13
[24]	515	Gauss	2	*Ra*			15.9		
[25]	535	Gauss	n.m.	*Ra*			14		16
[26]	1070	Gauss	n.m.	*Ra*					18
[27]	1064	Gauss	n.m.	*Ra*					12.72
[14, 28]	1070	Gauss	n.m.	*Ra*		19	15	15	12.21
[29]	1060–1100	Gauss	n.m.	*Ra*	27.6				
[68]	1064	Gauss	0	*Ra*			11.5		
			2	*Ra*			11.7*		
[69]	1064	Gauss	n.m.	*Sa*	74	26	13	12	
this study	1070	Gauss	2	*Sa*	33.09	23.44	10.19	11.93	
	1070	Ring (35/65)	2	*Sa*	30.05	18.56	17.04	34.16	
	1070	Ring (20/80)	2	*Sa*	25.63	16.44	24.31	36.29	
	1070	Ring (10/90)	2	*Sa*	25.41	16.81	22.78	38.53	
	1070	Gauss	2	*Sq*	42.52	29.75	12.91	15.82	
	1070	Ring (35/65)	2	*Sq*	37.72	23.71	21.68	44.89	
	1070	Ring (20/80)	2	*Sq*	32.18	21.18	30.49	44.54	
	1070	Ring (10/90)	2	*Sq*	32.52	21.52	28.83	46.99	

**With closest particle size distribution of 19–41 µm*

n.m. = not mentioned

Acknowledgements The authors would like to thank Christian Schröter from Optoprim Germany GmbH for providing the laser system. The provision is gratefully acknowledged.

Author Contributions Alexander Bauch: Conceptualization (lead); Data Curation; Formal analysis; Investigation; Methodology; Visualization; Resources (equal); Funding acquisition; Supervision; Writing - original draft. Philipp Kohlwes: Resources (equal); Writing – review & editing (equal); Conceptualization (support).Ingomar Kelbassa: Writing – review & editing (equal).

Funding Open Access funding enabled and organized by Projekt DEAL. The work described is partial financed with funds from the state innovation funding of the Free and Hanseatic City of Hamburg under the reference number LIF-004.

Data Availability The data that support the findings of this study are available from the corresponding author upon reasonable request.

Declarations

Competing Interests The work described is partial financed with funds from the state innovation funding of the Free and Hanseatic City of Hamburg under the reference number LIF-004. Optoprim Germany GmbH provided the laser system for a three-month period, but had no influence on the experiments, the analysis and publication of the results.

References

1. Bagehorn, S., Wehr, J., Maier, H.J.: Application of mechanical surface finishing processes for roughness reduction and fatigue improvement of additively manufactured Ti-6Al-4V parts. Int. J. Fatigue. (2017). https://doi.org/10.1016/j.ijfatigue.2017.05.008
2. Jiang, D., Tian, Y., Zhu, Y., Huang, A.: Investigation of surface roughness post-processing of additively manufactured nickel-based Superalloy Hastelloy X using electropolishing. Surf. Coat. Technol. (2022). https://doi.org/10.1016/j.surfcoat.2022.128529
3. Tyagi, P., Goulet, T., Riso, C., Stephenson, R., Chuenprateep, N., Schlitzer, J., Benton, C., Garcia-Moreno, F.: Reducing the roughness of internal surface of an additive manufacturing produced 316 steel component by chempolishing and electropolishing. Additive Manuf. (2019). https://doi.org/10.1016/j.addma.2018.11.001
4. Favero, G., Bonesso, M., Dima, R., Pepato, A., Zanini, F., Carmignato, S., Mancin, S.: Effect of the Building orientation on additively manufactured copper alloy: Hydraulic performance of different surface roughness channels. Int. J. Thermofluids. (2024). https://doi.org/10.1016/j.ijft.2024.100790
5. Mayerhofer, M., Brenner, S., Helm, R., Gruber, S., Lopez, E., Stepien, L., Gold, G., Dollinger, G.: Additive manufacturing of Side-Coupled cavity Linac structures from pure copper: A first concept. Instruments. (2023). https://doi.org/10.3390/instruments7040056
6. Tan, H.T., Lopez, E., Selbmann, A., Karl, D., Stepien, L., Brueckner, F.: Parameter analysis to correlate density with surface roughness and productivity in powder bed Fusion – Laser beam (PBF-LB) of AlSi10Mg. Procedia CIRP. (2024). https://doi.org/10.1016/j.procir.2024.08.090
7. Tian, Y., Tomus, D., Huang, A., Wu, X.: Experimental and statistical analysis on process parameters and surface roughness relationship for selective laser melting of Hastelloy X. Rapid Prototyp. J. (2019). https://doi.org/10.1108/RPJ-01-2019-0013
8. Tian, Y., Tomus, D., Rometsch, P., Wu, X.: Influences of processing parameters on surface roughness of Hastelloy X produced by selective laser melting. Additive Manuf. (2017). https://doi.org/10.1016/j.addma.2016.10.010
9. de Terris, T., Baffie, T., Ribière, C.: Additive manufacturing of pure copper: A review and comparison of physical, microstructural, and mechanical properties of samples manufactured with Laser-Powder bed fusion (L-PBF), electron beam melting (EBM) and metal fused deposition modelling (MFDM) technologies. Int. J. Mater. Form. (2023). https://doi.org/10.1007/s12289-023-01755-2
10. Bala, K., Pradhan, P.R., Saxena, N.S., Saksena, M.P.: Effective thermal conductivity of copper powders. J. Phys. D: Appl. Phys. (1989). https://doi.org/10.1088/0022-3727/22/8/009
11. Li, B.-Q., Li, Z., Bai, P., Liu, B., Kuai, Z.: Research on surface roughness of AlSi10Mg parts fabricated by laser powder bed fusion. Metals (2018). https://doi.org/10.3390/met8070524
12. Rott, S., Ladewig, A., Friedberger, K., Casper, J., Full, M., Schleifenbaum, J.H.: Surface roughness in laser powder bed fusion – Interdependency of surface orientation and laser incidence. Additive Manuf. (2020). https://doi.org/10.1016/j.addma.2020.101437

13. Spurek, M.A., Sillani, F., Haferkamp, L., Tosoratti, E., Spierings, A.B., Magazzeni, C.M., Meisnar, M., Wegener, K.: Effect of powder properties, process parameters, and recoating speed on powder layer properties measured by in-situ laser profilometry and part properties in laser powder bed fusion. Additive Manuf. (2024). https://doi.org/10.1016/j.addma.2024.104512
14. Sciacca, G., Sinico, M., Cogo, G., Bigolaro, D., Pepato, A., Esposito, J.: Experimental and numerical characterization of pure copper heat sinks produced by laser powder bed fusion. Mater. Design. (2022). https://doi.org/10.1016/j.matdes.2022.110415
15. Esmaeilizadeh, R., Ali, U., Keshavarzkermani, A., Mahmoodkhani, Y., Marzbanrad, E., Toyserkani, E.: On the effect of spatter particles distribution on the quality of Hastelloy X parts made by laser powder-bed fusion additive manufacturing. J. Manuf. Process. (2019). https://doi.org/10.1016/j.jmapro.2018.11.012
16. Wegner, J., Bruckhaus, L., Schroer, M.A., Rayer, M., Schoenrath, H., Kleszczynski, S.: Zr-based bulk metallic glasses in PBF-LB/M: near-polished surface quality in the as-built state. Prog Addit. Manuf. (2024). https://doi.org/10.1007/s40964-024-00667-0
17. Paradise, P., Patil, D., van Handel, N., Temes, S., Saxena, A., Bruce, D., Suder, A., Clonts, S., Shinde, M., Noe, C., Godfrey, D., Hota, R., Bhate, D.: Improving productivity in the laser powder bed fusion of inconel 718 by increasing layer thickness: Effects on mechanical behavior. J. Materi Eng. Perform. (2022). https://doi.org/10.1007/s11665-022-06961-8
18. Griemann, T., Söhnholz, N., Hoff, C., Hermsdorf, J., Kaierle, S.: Adjusting the surface roughness of WE43 components manufactured by laser-based powder bed fusion adjusting the surface roughness of WE43 components manufactured by laser-based powder bed fusion. Lasers Manuf. Converence (2021). 2021 (LIM2021)
19. Charles, A., Elkaseer, A., Paggi, U., Thijs, L., Hagenmeyer, V., Scholz, S.: Down-facing surfaces in laser powder bed fusion of Ti6Al4V: Effect of Dross formation on dimensional accuracy and surface texture. Additive Manuf. (2021). https://doi.org/10.1016/j.addma.2021.102148
20. Vu, H.M., Meiniger, S., Ringel, B., Hoche, H., Oechsner, M., Weigold, M., Seidel, C.: Investigation on surface characteristics of wall structures out of stainless steel 316L manufactured by laser powder bed fusion. Prog Addit. Manuf. (2024). https://doi.org/10.1007/s40964-023-00559-9
21. de Terris, T., Baffie, T., Ribiere, C.: Comparison of two methods to manufacture pure copper by laser-powder bed fusion (L-PBF). Euro PM2021 - European Metallurgy Conference, Grenoble, France, Oct. (2021)
22. Gruber, S., Stepien, L., López, E., Brueckner, F., Leyens, C.: Physical and geometrical properties of additively manufactured pure copper samples using a green laser source. Mater. (Basel Switzerland). (2021). https://doi.org/10.3390/ma14133642
23. Jadhav, S.D., Goossens, L.R., Kinds, Y., van Hooreweder, B., Vanmeensel, K.: Laser-based powder bed fusion additive manufacturing of pure copper. Additive Manuf. (2021). https://doi.org/10.1016/j.addma.2021.101990
24. Domine, A., Verdy, C., Penaud, C., Vitu, L., Fenineche, N., Dembinski, L.: Selective laser melting (SLM) of pure copper using 515-nm green laser: From single track analysis to mechanical and electrical characterization. Int. J. Adv. Manuf. Technol. (2023). https://doi.org/10.1007/s00170-023-12338-5
25. Ning, Z., Hu, H., Zhao, T., Wang, S., Song, M.: Enhanced electrical and mechanical properties of additively manufactured pure copper with green laser. J. Mater. Process. Technol. (2024). https://doi.org/10.1016/j.jmatprotec.2024.118615
26. Constantin, L., Wu, Z., Li, N., Fan, L., Silvain, J.-F., Lu, Y.F.: Laser 3D printing of complex copper structures. Additive Manuf. (2020). https://doi.org/10.1016/j.addma.2020.101268
27. Yan, X., Chang, C., Dong, D., Gao, S., Ma, W., Liu, M., Liao, H., Yin, S.: Microstructure and mechanical properties of pure copper manufactured by selective laser melting. Mater. Sci. Engineering: A. (2020). https://doi.org/10.1016/j.msea.2020.139615
28. Sinico, M., Cogo, G., Benettoni, M., Calliari, I., and A. Pepato (eds.): Proceedings of the 30th Annual International (2019) (2019)
29. Candela, V., Pozzi, M., Chyhyrynets, E., Garcia Diaz, V., Candela, S., Dima, R., Favero, G., Pira, C., Pepato, A., Sonato, P.: Smoothening of the down-skin regions of copper components produced via laser powder bed fusion technology. Int. J. Adv. Manuf. Technol. (2022). https://doi.org/10.1007/s00170-022-10408-8
30. Bauch, A., Kohlwes, P., Kelbassa, I.: Laser powder bed fusion of pure copper using ring-shaped beam profiles. J. Laser Appl. (2024). https://doi.org/10.2351/7.0001562

31. Bauch, A., Herzog, D.: Influence of temperature and beam size on weld track shape in laser powder bed fusion of pure copper using near-infrared laser system. J. Laser Appl. (2024). https://doi.org/10.2351/7.0001118
32. Fabbro, R., Dal, M., Peyre, P., Coste, F., Schneider, M., Gunenthiram, V.: Analysis and possible Estimation of keyhole depths evolution, using laser operating parameters and material properties. J. Laser Appl. (2018). https://doi.org/10.2351/1.5040624
33. Han, L., Liou, F.W.: Numerical investigation of the influence of laser beam mode on melt pool. Int. J. Heat Mass Transf. (2004). https://doi.org/10.1016/j.ijheatmasstransfer.2004.04.036
34. Khairallah, S.A., Anderson, A.T., Rubenchik, A., King, W.E.: Laser powder-bed fusion additive manufacturing: Physics of complex melt flow and formation mechanisms of pores, spatter, and denudation zones. Acta Mater. (2016). https://doi.org/10.1016/j.actamat.2016.02.014
35. Wischeropp, T.M.: Advancement of selective laser melting by laser beam shaping. Dissertation, Hamburg University of Technology (2022)
36. Bayat, M., Rothfelder, R., Schwarzkopf, K., Zinoviev, A., Zinovieva, O., Spurk, C., Hummel, M., Olowinsky, A., Beckmann, F., Moosmann, J., Schmidt, M., Hattel, J.H.: Exploring Spatial beam shaping in laser powder bed fusion: High-fidelity simulation and in-situ monitoring. Additive Manuf. (2024). https://doi.org/10.1016/j.addma.2024.104420
37. Holla, V., Kopp, P., Grünewald, J., Wudy, K., Kollmannsberger, S.: Laser beam shape optimization in powder bed fusion of metals. Additive Manuf. (2023). https://doi.org/10.1016/j.addma.2023.103609
38. Dai, R., Yang, B., Wudy, K.: Impact of beam shaping on melt pool behavior in laser processing of stainless steel 316L: Thermal analysis using multispectral imaging. J. Mater. Process. Technol. (2025). https://doi.org/10.1016/j.jmatprotec.2025.118835
39. Pérez-Ruiz, J.D., Galbusera, F., Caprio, L., Previtali, B., de Lacalle, L.N.L., Lamikiz, A., Demir, A.G.: Laser beam shaping facilitates tailoring the mechanical properties of IN718 during powder bed fusion. J. Mater. Process. Technol. (2024). https://doi.org/10.1016/j.jmatprotec.2024.118393
40. Guo, Q., Zhao, C., Escano, L.I., Young, Z., Xiong, L., Fezzaa, K., Everhart, W., Brown, B., Sun, T., Chen, L.: Transient dynamics of powder spattering in laser powder bed fusion additive manufacturing process revealed by in-situ high-speed high-energy x-ray imaging. Acta Mater. (2018). https://doi.org/10.1016/j.actamat.2018.03.036
41. Young, Z.A., Guo, Q., Parab, N.D., Zhao, C., Qu, M., Escano, L.I., Fezzaa, K., Everhart, W., Sun, T., Chen, L.: Types of spatter and their features and formation mechanisms in laser powder bed fusion additive manufacturing process. Additive Manuf. (2020). https://doi.org/10.1016/j.addma.2020.101438
42. Kohlwes, P.: Prozessstabile additive Fertigung durch spritzerreduziertes Laserstrahlschmelzen. Doctoral dissertation, Hamburg University of Technology (2024)
43. Grünewald, J., Gehringer, F., Schmöller, M., Wudy, K.: Influence of Ring-Shaped beam profiles on process stability and productivity in Laser-Based powder bed fusion of AISI 316L. Metals. (2021). https://doi.org/10.3390/met11121989
44. Nahr, F., Bartels, D., Rothfelder, R., Schmidt, M.: Influence of novel beam shapes on Laser-Based processing of High-Strength aluminium alloys on the basis of EN AW-5083 single weld tracks. JMMP (2023). https://doi.org/10.3390/jmmp7030093
45. Cozzolino, E., Tiley, A.J., Ramirez, A.J., Astarita, A., Herderick, E.D.: Energy efficiency of Gaussian and ring profiles for LPBF of nickel alloy 718. Int. J. Adv. Manuf. Technol. (2024). https://doi.org/10.1007/s00170-024-13511-0
46. Yu, T., Zhao, J.: Quantitative simulation of selective laser melting of metals enabled by new high-fidelity multiphase, multiphysics computational tool. Comput. Methods Appl. Mech. Eng. (2022). https://doi.org/10.1016/j.cma.2022.115422
47. Zöller, C., Adams, N.A., Adami, S.: Beam-shaping in laser-based powder bed fusion of metals: A computational analysis of point-ring intensity profiles. Additive Manuf. (2024). https://doi.org/10.1016/j.addma.2024.104402
48. Glaubitz, E.B., Fox, J.C., Kafka, O.L., Gockel, J.: Contour parameters, melt pool behavior, and surface roughness relationships across laser powder bed fusion platforms and metallic alloys. Int. J. Adv. Manuf. Technol. (2025). https://doi.org/10.1007/s00170-025-15066-0
49. Kranz, J., Herzog, D., Emmelmann, C.: Design guidelines for laser additive manufacturing of lightweight structures in TiAl6V4. J. Laser Appl. (2015). https://doi.org/10.2351/1.4885235
50. Galbusera, F., Caprio, L., Previtali, B., Demir, A.G.: Analytical modeling and characterization of ring beam profiles for high-power lasers used in industrial manufacturing. J. Manuf. Process. (2024). https://doi.org/10.1016/j.jmapro.2024.02.069

51. Chen, H., Gu, D., Xiong, J., Xia, M.: Improving additive manufacturing processability of hard-to-process overhanging structure by selective laser melting. J. Mater. Process. Technol. (2017). https://doi.org/10.1016/j.jmatprotec.2017.06.044
52. Li, X., Zhao, C., Sun, T., Tan, W.: Revealing transient powder-gas interaction in laser powder bed fusion process through multi-physics modeling and high-speed synchrotron x-ray imaging. Additive Manuf. (2020). https://doi.org/10.1016/j.addma.2020.101362
53. Feng, Y., Gao, X., Zhang, Y., Peng, C., Gui, X., Sun, Y., Xiao, X.: Simulation and experiment for dynamics of laser welding keyhole and molten pool at different penetration status. Int. J. Adv. Manuf. Technol. (2021). https://doi.org/10.1007/s00170-020-06489-y
54. Yuan, J., Guo, Q., Clark, S.J., Escano, L.I., Nabaa, A., Qu, M., Huang, J., Li, Q., Román, A.J., Osswald, T.A., Fezzaa, K., Chen, L.: Revealing mechanisms of processing defect mitigation in laser powder bed fusion via shaped beams using high-speed X-ray imaging. Int. J. Mach. Tools Manuf. (2025). https://doi.org/10.1016/j.ijmachtools.2024.104232
55. Cunningham, R., Zhao, C., Parab, N., Kantzos, C., Pauza, J., Fezzaa, K., Sun, T., Rollett, A.D.: Keyhole Threshold and Morphology in Laser Melting Revealed by ultrahigh-speed x-ray Imaging. Science, New York, N.Y.) (2019). https://doi.org/10.1126/science.aav4687
56. Khairallah, S.A., Martin, A.A., Lee, J.R.I., Guss, G., Calta, N.P., Hammons, J.A., Nielsen, M.H., Chaput, K., Schwalbach, E., Shah, M.N., Chapman, M.G., Willey, T.M., Rubenchik, A.M., Anderson, A.T., Wang, Y.M., Matthews, M.J., King, W.E.: Controlling Interdependent meso-nanosecond Dynamics and Defect Generation in Metal 3D Printing. Science, New York, N.Y.) (2020). https://doi.org/10.1126/science.aay7830
57. Matthews, M.J., Guss, G., Khairallah, S.A., Rubenchik, A.M., Depond, P.J., King, W.E.: Denudation of metal powder layers in laser powder bed fusion processes. Acta Mater. (2016). https://doi.org/10.1016/j.actamat.2016.05.017
58. Chen, H., Yan, W.: Spattering and denudation in laser powder bed fusion process: Multiphase flow modelling. Acta Mater. (2020). https://doi.org/10.1016/j.actamat.2020.06.033
59. Bidare, P., Bitharas, I., Ward, R.M., Attallah, M.M., Moore, A.J.: Fluid and particle dynamics in laser powder bed fusion. Acta Mater. (2018). https://doi.org/10.1016/j.actamat.2017.09.051
60. Yadroitsev, I., Gusarov, A., Yadroitsava, I., Smurov, I.: Single track formation in selective laser melting of metal powders. J. Mater. Process. Technol. (2010). https://doi.org/10.1016/j.jmatprotec.2010.05.010
61. Skalon, M., Meier, B., Gruberbauer, A., Amancio-Filho, S.T., Sommitsch, C.: Stability of a melt pool during 3D-Printing of an unsupported steel component and its influence on roughness. Mater. (Basel Switzerland). (2020). https://doi.org/10.3390/ma13030808
62. Gargalis, L., Ye, J., Strantza, M., Rubenchik, A., Murray, J.W., Clare, A.T., Ashcroft, I.A., Hague, R., Matthews, M.J.: Determining processing behaviour of pure Cu in laser powder bed fusion using direct micro-calorimetry. J. Mater. Process. Technol. (2021). https://doi.org/10.1016/j.jmatprotec.2021.117130
63. Nordet, G., Gorny, C., Coste, F., Lapouge, P., Effernelli, A., Blanchet, E., Peyre, P.: Influence of laser wavelength on the powder bed fusion of pure copper. Prog Addit. Manuf. (2025). https://doi.org/10.1007/s40964-024-00720-y
64. Mohr, G., Sommer, K., Knobloch, T., Altenburg, S.J., Recknagel, S., Bettge, D., Hilgenberg, K.: Process induced preheating in laser powder bed fusion monitored by thermography and its influence on the microstructure of 316L stainless steel parts. Metals (2021). https://doi.org/10.3390/met11071063
65. Wischeropp, T.M., Emmelmann, C., Brandt, M., Pateras, A.: Measurement of actual powder layer height and packing density in a single layer in selective laser melting. Additive Manuf. (2019). https://doi.org/10.1016/j.addma.2019.04.019
66. Ninpetch, P., Chalermkarnnon, P., Kowitwarangkul, P.: Multiphysics simulation of Thermal-Fluid behavior in laser powder bed fusion of H13 steel: Influence of layer thickness and energy input. Met. Mater. Int. (2023). https://doi.org/10.1007/s12540-022-01239-z
67. Yang, J., Han, J., Yu, H., Yin, J., Gao, M., Wang, Z., Zeng, X.: Role of molten pool mode on formability, microstructure and mechanical properties of selective laser melted Ti-6Al-4V alloy. Mater. Design. (2016). https://doi.org/10.1016/j.matdes.2016.08.036
68. Bonesso, M., Rebesan, P., Gennari, C., Mancin, S., Dima, R., Pepato, A., Calliari, I.: Effect of particle size distribution on laser powder bed fusion manufacturability of copper. Berg Huettenmaenn. Monatsh. (2021). https://doi.org/10.1007/s00501-021-01107-0

69. EOS GmbH: EOS Copper CuCP - Material Data Sheet. (2025). https://www.eos.info/var/assets/05-datasheet-images/Assets_MDS_Metal/EOS_Copper_CuCP/Material_DataSheet_EOS%20_Copper_CuCP_en.pdf?v=5. Accessed 11 April 2025

Authors and Affiliations

Alexander Bauch[1] · Philipp Kohlwes[1] · Ingomar Kelbassa[1,2]

✉ Alexander Bauch
alexander.bauch@iapt.fraunhofer.de

[1] Fraunhofer Research Institution for Additive Manufacturing Technologies IAPT, Am Schleusengraben 14, 21029 Hamburg, Germany

[2] Institute for Industrialization of Smart Materials (ISM), Hamburg University of Technology, Harburger Schloßstraße 28, 21079 Hamburg, Germany